Petroleum Science 19 (2022) 2326–2342

Contents lists available at ScienceDirect

Petroleum Science

journal homepage: www.keaipublishing.com/en/journals/petroleum-science

Original Paper

Experimental investigation of tubing collar's influence on hydrodynamic behavior of annular duct flow

Yi-Su Zhou [a], Zhong-Wei Huang [a, *], Zhuang-Zhuang Zhang [a], Tian-Wen Jiang [a], Rui-Yue Yang [a], Ming-He Zhang [b]

[a] State Key Laboratory of Petroleum Resources and Prospecting, China University of Petroleum Changping, Beijing 102249, China
[b] China University of Petroleum (Beijing), Changping, Beijing 102249, China

ARTICLE INFO

Article history:
Received 9 January 2022
Received in revised form
1 April 2022
Accepted 1 April 2022
Available online 30 April 2022

Edited by Xiu-Qiu Peng

Keywords:
Variable cross-section annulus flow
Sudden contraction and expansion
Hydrodynamic behavior
PIV
POD

ABSTRACT

Tubing collars' influence on hydrodynamic behavior of annular duct flow has been investigated using Particle Image Velocity (PIV) technology. PIV has become an efficient method for complex transient flows visualization. A water flow loop with two replaceable variable cross-sections (VCS), 75−90 mm and 90−110 mm, in a 129 mm inner diameter (ID) pipe was used. The whole field of the variable cross-section annulus (VCSA) was visualized, including forward-facing step (FFS), narrow annulus (NA), and backward-facing step (BFS) flow. The VCSA ratio and Reynolds (Re) number influence on streamline distribution, velocity distribution, and turbulence intensity were discussed. Results showed that the recirculation is easier to form in BFS than FFS flow under the same condition. The VCSA ratio affects the formation of recirculation zones and the location of the reattachment point. Reynolds number mainly affects BFS flow by influencing the main velocity component - axial velocity. The turbulence intensity is relatively high in BFS than FFS flow and is larger at $y/h>1.0$ than $y/h<1.0$. Furthermore, the streamwise coherent structures reveal that the first two modes are predominant and represent the main characteristics of the flow by proper orthogonal decomposition (POD) method.

1. Introduction

With the development of deep wells and ultra-deep wells, improper prediction and control of pressure frequently pose significant challenges, which seriously affect the cost and safety in the petroleum industry (Dokhani et al., 2020; Qin et al., 2021). Precise prediction of annular pressure losses is one of the most critical challenges, including drilling, completion, fracturing, acidizing, workover and production (Jeong and Subhash, 2004; Birchenko et al., 2010). This becomes more vital and sophisticated with the increase of well depth, not only by the effects of rotation, eccentricity, and fluid properties but also by the increasing number of tubing collars and tool joints. The presence of a tubing collar or a tool joint changes the annulus geometry resulting in strong turbulence and fluid acceleration that generates additional pressure losses (Enfis et al., 2011). Drill pipes and tubings are connected by tool joints and tubing collars with larger diameters separately, leading to tapered (gradual) and squared (sudden) contraction-expansion zones in the annulus, both resulting in extra pressure losses which cannot be neglected. The effect of tool joints and tubing collars in flow can be regarded as the flow past wall-mounted finite cylinders (both circular and square). Many engineering configurations (Sachidananda and Arun. 2021; Woyciekoski et al., 2020; Ma et al., 2020; Yuan et al., 2020), such as heat-exchangers, several building structures and electronic cooling systems of environment can be also regarded as finite-length cylinders. Therefore, this particular flow configuration has received a lot of attention in recent years due to its importance in engineering applications and fundamental research. The flow field of forward-backward facing step (FBFS) geometry with a plate boundary has been investigated in many previous works with higher Re numbers (Sazhin, 2021; Chalmers et al., 2020; Addad et al., 2003). Fang and Tachie. (2019) performed a FBFS of an intermediate aspect to study the turbulence structures using a time-resolved PIV. Recently, Malah et al. (2021) numerically described the effects of the cross-section shape of the cylinder, which included square, circular and

* Corresponding author.
E-mail address: huangzw@cup.edu.cn (Z.-W. Huang).

https://doi.org/10.1016/j.petsci.2022.04.001

prismatic cylinders on the dynamics characteristics of the vortex system.

Several theoretical, numerical, and experimental investigations have been conducted to explain tool joints' and tubing collars' effect on the frictional pressure losses in annulus flow. Cartalosu and Dupuis (1993) noted that the variations in annular clearance, such as tool joints, have consequences on the annular pressure losses in slim holes. They presented a simple model which considered the tool joint as a part of the annulus with different pipe sizes to account for the tool joints' effect on pressure loss. The influence of tool joints on pressure losses was investigated (Wang and Bai, 1998) by a slim hole annulus experiment. The experimental data showed that the effect of tool joints on slim hole annulus pressure losses is significant. The pressure losses increased sharply with a high-speed rotating drill pipe. Jeong and Subhash (2004) presented the experimental data with three different fluids and discussed the results of tool joints' effect on the annular pressure loss. The authors found that the presence of tool joints on the annular friction pressure is significant and a prediction method for annular pressure loss was proposed. Ochoa. (2006) proposed five approaches to correct pump pressure losses by considering tool joints and gave an example of how these approaches worked. It concluded that a tool joint increases pressure losses in the annulus due to geometry effects. The proposed correcting methods for predicting pressure losses suited different fluid properties. Hemphill et al. (2007) studied the distribution of pressure losses, including the rotating drill pipe, the rotating tool joints, and the rotating drill collars. It indicated that the tool joints effect could be as high as 12% of the total annular pressure loss. Simoes et al. (2007) evaluated the influence of the tool joints on equivalent circulating density (ECD) for different wellbore geometries, drilling fluids and flow rates through the computational fluid dynamics (CFD) technique. Additional pressure loss was observed caused by the presence of tool joints and the abrupt tool joints caused higher pressure losses than gradual. It was also observed that pressure losses were reduced with increased eccentricity. Enfis et al. (2011) investigated the hydraulic effects of rotating and non-rotating tool joints. The authors found that a substantial increase in pressure loss was around the tool joints, which depended on fluid properties and flow geometries and the rotation of the pipe effect was slight. Bui (2012) used CFD software to simulate different influencing factors on annular pressure losses with tool joints. It is found that pipe rotation had a smaller effect on pressure drop at lower velocity. Flow geometry and flow velocity were the main influencing factors on both positive and negative effects strongly. Dokhani et al. (2020) investigated the flow around squared and tapered tool joints by a CFD approach. Simulation results indicated squared tool joints increased the pressure loss up to 42%, and tapered tool joints increased the pressure loss up to 26%. Vajargah et al. (2014) compared the pressure losses in the annulus with and without tool joints to investigate the tool joints effect by CFD software using finite volume methods (FVM). The author found that the ratio of annular pressure losses with tool joints to one without tool joints strongly depended on the flow regime. Huang et al. (2015) designed experimental equipment according to the actual size of the tubing and casing in the oilfield. The investigation tested and analyzed the pressure losses in the annulus under the conditions of placing different sizes of tubing, different numbers, and sizes of couplings in the casing. The annular pressure loss was approximately linear with the number of couplings and was a quadratic function of the pump inflow by linear regression. Eren (2018) summarized a literature review regarding the effects of tool joints during drilling. In this study, the tool joints' effect on the dill pipe of Middle East formations were taken into consideration to calculate pressure losses in the annulus and ECD. And partial results were compared to previous investigations. The hydrodynamics in an annular channel with tool joint was simulated and Orlik et al. (2020) found that the separation area decreased with the increase Re numbers. Recently, a methodology was used to investigate the effect of casing couplings on ECD (Eren et al., 2021) which was a step-change for automation in drilling operations. This research study revealed that annular frictional pressure losses were significant for successful casing running operations during circulations and at the time of the cementing of the same. A modified open-hole extended-reach limit model was presented (Zhu et al., 2021) considering the hydraulic effect of tool joints. Three typical, two well types and fluid properties were analyzed. The previous works focused on the VCS effect on the annular frictional pressure losses are listed in Table 1.

Previous studies have been conducted to explain the effect of the tool joints and tubing collars on the frictional pressure losses in the annulus. It should be noted that a detailed study of VCS effects on hydrodynamics in the annulus has not been carried out. In this paper, the annular flow with a tubing collar, which has the sudden contraction-expansion structure in the annulus, is called variable cross-section annulus flow. Many downhole tools have similar VCS structures in the annulus. But few works have investigated the flow characteristics in the annulus, and the flow characteristics of VCS in the annulus are still unclear. A single segment of a tubing collar may not result in excessive pressure loss individually. However, the sum of the frictional pressure losses for all tubing collars could result in additional significant frictional pressure losses with the increase of well depth. Therefore, it is of great significance to grasp the VCSA flow characteristics to explore its influence on frictional pressure losses further.

Methods for flow visualization have been decisive for the historical development of fluid mechanics (Rodolfo et al., 2021). Many experimental investigations have been conducted to obtain and explain the flow field data in the oil industry's annulus and fluid machine. The PIV measurement technique is considered an effective method for flow visualization. Experimental studies were conducted to investigate bed erosion parameters and flow characteristics in horizontal annulus using the PIV system (Hirpa et al., 2020; Hirpa and Ergun, 2020; Bizhani and Kuru. 2018; Bizhani and Kuru, 2018). PIV was widely used in the visualization of fluid machines, such as hydro-cyclones and centrifugal pumps (Li et al., 2020; Araújo et al., 2013), to measure the inside velocity for a further complex explanation.

The limitations of previous works motivate this paper. This paper investigated the VCSA flow characteristics and the influence factors, such as geometry structure and Re number using the PIV visualization method. The structure of the paper is organized as follows. In section 2, the experimental setup and test procedure are introduced; the flow visualization results, influencing factors on VCSA flow characteristics and vorticity-based POD have been discussed in Section 3; conclusions are drawn in Section 4.

2. Experimental setup and test procedure

2.1. VCSA model

The design of the VCSA model followed almost the same dimensions of the casing annulus with a tubing collar in the field. The inner diameter of the outer pipe was 129 mm closed to $5^{1/2'}$ casing and remained unchanged during the experiment. The diameters of VCS were 90 mm and 110 mm, which matched the two 75 mm and 90 mm inner pipe diameters, separately. The inner pipes with the VCS were very closed to $2^{7/8'}$ and $3^{1/2'}$ tubing on site. The subscribed 1 and 2 represented the 75 mm and 90 mm inner pipe, respectively. Fig. 1 schematically illustrated the VCSA geometry and the X–Y plane (Z=0) which was mainly investigated in this paper.

Table 1
Summary of past works focused on the VCS structure effect on the annulus frictional pressure losses.

Reference	Approach	Influencing factors	VCS types
Cartalosu and Dupuis (1993)	Theoretical	Annular gap geometries	Tool joint
Wang and Bai (1998)	Experimental	Flow rates, fluid properties, and annular gap geometries	Tool joint (tapered)
Jeong and Subhash (2004)	Experimental	Flow rates, fluid properties, and Re	Tool joint (squared)
Viloria and Marilyn. (2006)	Theoretical	Flow rates and fluid properties	Tool joint (tapered)
Hemphill et al. (2007)	Theoretical	Pipe rotation	Tool joint (tapered)
Simoes et al. (2007)	Theoretical and numerical	Flow rates, fluid properties tool joints angles, and eccentricity	Tool joint (tapered and squared)
Enfis et al. (2011)	Theoretical and experimental	Flow rates, fluid properties, pipe rotation, Re, and annular gap geometries	Tool joint (tapered)
Bui (2012)	Numerical	Flow rates, pipe rotation, and eccentricity	Tool joint (squared)
Dokhani et al. (2020)	Numerical	Annular gap geometries	Tool joint (squared)
Vajargah et al. (2014)	Numerical	Flow rates, fluid properties, Re, and annular gap geometries	Tool joint (squared)
Huang et al. (2015)	Experimental and numerical	Flow rates, number of couplings, annular gap, and geometries	Tubing collar (squared)
Eren (2018)	Numerical	Flow rates, fluid properties, and well depth	Tool joint (tapered and squared)
Orlik et al. (2020)	Numerical	Eccentricity, pipe rotation, Re, and annular gap geometries	Tool joint (tapered)
Eren et al. (2021)	Numerical	Flow rates, fluid properties, and annular gap geometries	Casing coupling (squared)
Zhu et al. (2021)	Theoretical	Tree major drilling conditions, fluid properties, and two well types	Tool joint (tapered and squared)

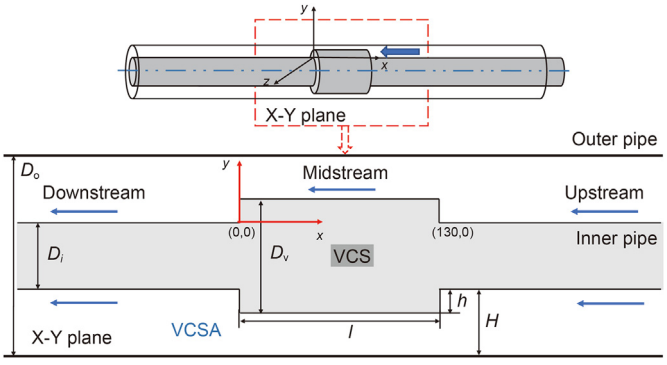

Fig. 1. Schematic diagram of VCSA model and the Cartesian system of X–Y plane.

H is half of the hydraulic diameter, l is the length of VCS and h/H is defined as the VCSA ratio. The parameters of the VCSA model are shown in Table 2. The two variable cross-section annulus are named 90–129 mm VCSA and 110–129 mm VCSA which contains the 75–90 mm and 90–110 mm VCS, corresponding to the geometric dimensions separately.

2.2. Experimental setup

A schematic diagram of the entire horizontal annular duct flow loop used in the experimental study is shown in Fig. 2. A large-scale wellbore simulator composed of an 8.5 m long annular section in which fluid was fully developed. The flow loop was comprised of a 300 L capacity suction tank, an observation section, a centrifugal pump (SRM100BZ-20), a magnetic flowmeter with an accuracy of ±0.5% (ASMIK LDG-SUP-DN100), several gate valves to control the fluid flow, a data acquisition system (ART DAM-3154 and DAM-3232 N), and suction and discharge lines. The outer pipe and the observation section of the flow loop were made out of polymethyl methacrylate, and the inner pipe was made out of PVC material to reduce the weight of the experimental device. The outer test section was composed of four 2 m long pipes connected by square flanges and the inner test section was connected using specially designed inner joints. The inner pipe was centralized in the annulus by supporting both ends.

Fig. 3 illustrates the flow loop equipped with a PIV system for velocity field measurement. As shown in Fig. 3, the flow loop was positioned inside a rectangular polymethyl methacrylate box filled with glycerol. Glycerol and the polymethyl methacrylate pipe had a similar refractive index. This arrangement allowed the laser light to impinge upon the fluid orthogonally. It minimized the measurement errors arising from the glass pipe's circular shape, causing refraction of the laser light. The PIV system from Dantec consisted of a double-pulsed laser [Neodymium-doped Yttrium Aluminum Garnet (Nd: YAG)], a LaVision Imager Intense CCD camera [Nikon 50-mm f/1.4 AF Nikkor™ lens (Nikon Corp., Tokyo, Japan)], a synchronizer, a guiding beam arm, and commercial processing software (Dynamics Studio 6.11) for controlling the PIV measurements and obtaining the velocity fields. The imager tense was a double-framed camera with a 12-bit CCD sensor. The wavelength of the laser was 532 nm and the pulse duration was 4 ns. The trigger rate was the sampling frequency of the PIV setup depended on the lowest frequency of the camera and laser which was 15 Hz in this experiment. The time between pulse (Δt) ranged from 3000 to 8000 μs according to different flow rates which was the time difference between the two particle images.

2.3. Experimental procedure

The experimental procedure consisted of four steps. The annulus with constant cross-section were control groups. Before the experiment, 5 μm diameter Polyamid Seeding Particles (PSP) were added to the fluid as tracking particles for reflecting the laser. Compared with traditional tracking particles, the surface of PSP improved the reflection intensity of particles and the density of it was 1.03–1.05 g/cm^3 which was close to the water density and hard

Table 2
Parameters of the VCSA model used in the experiment.

90–129 mm VCSA parameters	Value	110–129 mm VCSA parameters	Value
Outer pipe diameter (Do)	129 mm	Outer pipe diameter (Do)	129 mm
Inner pipe 1 diameter (D_{i1})	75 mm	Inner pipe 2 diameter (D_{i2})	90 mm
VCS 1 diameter (Dv_1)	90 mm	VCS 2 diameter (Dv_2)	110 mm
Step height 1 (h_1)	7.5 mm	Step height 2 (h_2)	10 mm
Hydraulic Diameter 1 (D_{H1})	54 mm	Hydraulic Diameter 2 (D_{H2})	39 mm
VCS 1 length (lv_1)	130 mm	VCS 2 length (lv_2)	130 mm
VCSA ratio 1 (h_1/H_1)	0.28	VCSA ratio 2 (h_2/H_2)	0.51

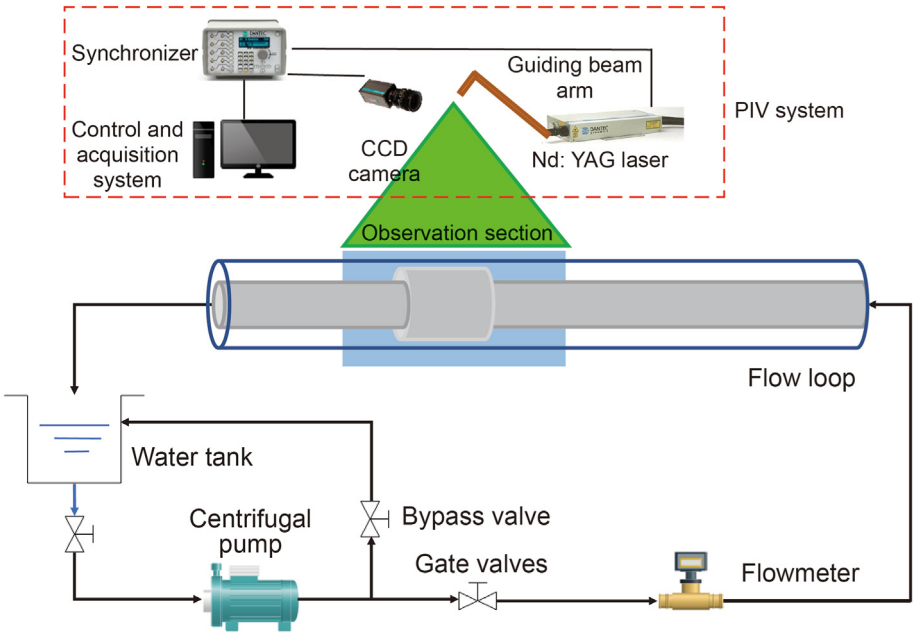

Fig. 2. The schematic diagram for the entire experimental flow loop.

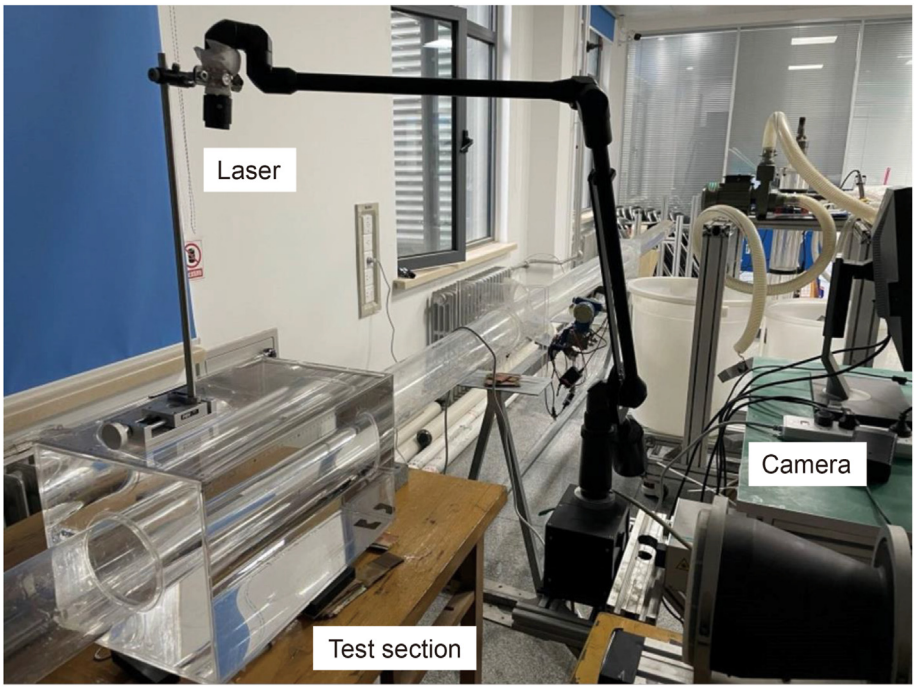

Fig. 3. Image of the PIV setup and test section.

to settle.

(1) The first step was water circulation in the constant cross-section annulus and obtaining flow field data by PIV at 1, 3, 5, 6 m^3/h flow rate for 75–129 mm constant annulus;
(2) The second step was to install the 75–90 mm VCS on the 75 mm inner diameter pipe. Open the valves to control the flow rate at 1 m^3/h. By adjusting the camera and laser, the FFS flow, NA flow, and BFS flow were measured, respectively. That is to say, the measurement of the whole flow field data needed to be carried out three times at one specific flow rate. And then repeated the above operations for velocity data obtained at the flow rate of 3, 5, 6 m^3/h;
(3) The third step was to replace the 75 mm ID pipe with the 90 mm ID pipe. The water circulation in the 90–129 mm constant cross-section annulus and obtaining flow field data by PIV at 1 m^3/h, 3 m^3/h, 5 m^3/h, 6 m^3/h flow rate;
(4) The fourth step was to install the 90–110 mm VCS on the 90 mm ID pipe. Open the valves to control the flow rate at 1 m^3/h. By adjusting the camera and laser, the FFS flow, NA flow, and BFS flow were measured, respectively. And then

repeated the above operations for velocity data obtained at the flow rate of 3, 5, 6 m^3/h.

3. Results and discussion

3.1. Flow visualization in VCSA

One of the essential results of the experimental investigation is the visualization of the whole flow field of VCSA, which is divided into upstream FFS flow, midstream NA flow, and downstream BFS flow. The 2D and 3D streamline contours have been indicated to be almost identical in various VCS structures, such as cavity geometry (Veeresh and Venkatasubbaiah. 2021). To simplify the operation, we only investigated the 2D-2C (two-dimensional planar) flow field characteristics in the X–Y plane (Z=0) in this paper. Figs. 4–5 showed and compared the vector maps in three different zones at the flow rate of 5 m^3/h for 90–129 mm and 110–129 mm VCSA, respectively. The different colors in the figure represented the mean velocity vectors value. From Figs. 4b and 5b, the vectors were paralleled with the flow direction for NA flow, almost identical to the vectors map in Fig. 6. The vectors of NA flow only increased and then decreased at the FFS entrance. However, the vectors dramatically changed in FFS and BFS flow as shown in Figs. 4–5a and 4-5c. For FFS flow, it can be observed that no separated turbulent vortex was produced at the FFS corner neither in 90–129 mm nor 110–129 mm VCSA, though the formation tendency of the vortex was apparent. For BFS flow, it can be observed that two large-scale separated turbulent vortexes produced behind BFS. The phenomenon indicated that the generation of recirculation zone in BFS was easier than FFS under the same condition. The size and number of recirculation zone of BFS flow were larger than FFS flow, though both BFS and FFS had the same VCSA ratio.

Fig. 6 showed the time-averaged vector maps at the flow rate of 5 m^3/h for smooth annulus flow. Treatment groups were studied to compare the flow field in an annular casing duct with and without a tubing collar. No recirculation zones founded, the flow field of the smooth annulus was steady and fully developed compared to the VCSA flow. This means the presence of tubing collars makes flow field disturbance causing extra pressure losses, namely local head loss. The local head losses are calculated as follows by Eq. (1) and Eq. (2):

$$A_1v_1 = A_2v_2, A_2v_2 = A_3v_3 \tag{1}$$

$$h_{jc} = \frac{(v_1 - v_2)^2}{2g}, h_{je} = \frac{(v_2 - v_3)^2}{2g} \tag{2}$$

Where v_1, v_2, v_3 and are mean velocities in A_1, A_2, A_3 and cross-sections separately. h_{je} and h_{jc} represent the expansion head loss and contraction head loss.

According to Eqs. (1) and (2), the h_{jc} is equal to h_{je}, h_{je} but the is smaller than h_{jc} due to the different size of recirculation zones actually through the PIV visualization flow field. That is, the local head losses due to sudden contraction were equal to the sudden expansion when the flow conditions were certain in an annular with a tubing collar. However, pressure losses of the BFS flow were smaller than the FFS flow. Kaushik et al., (2012) and Yao et al., (2019) studied the local head losses in a contraction and expansion pipe and obtained a similar law. The flow visualization provides a theoretical basis for pressure losses calculation.

The schematic diagram of the whole flow field model of VCSA was shown in Fig. 7. The flow field of VCSA was similar to FBFS in the X–Y plane (Abu-Mulaweh, 2009). The influence of the outer pipe wall on the main flow area and recirculation zone in the X–Y plane of VCSA flow was not obvious.

3.2. Effects of VCSA ratio

3.2.1. Streamline distribution

The VCSA ratio characterizes the proportion of the step height in the annular clearance. The BFS and FFS streamline distribution for the VCSA ratio=0.28 and 0.51 at the flow rate of 1 m^3/h were depicted in Figs. 8 and 9. From Figs. 8 and 9, the formation of two different recirculation zones in the BFS flow can be seen. The phenomenon also occurred in BFS flow (Yang et al., 2021; Ma et al., 2021; McQueen et al. 2021) with different fluids properties. In Fig. 9, the vortex zone in which the streamline direction was consistent with the flow direction was defined as the primary recirculation zone, and the secondary recirculation was contrary to it. The reattachment length was at -3.75<x/h< -2.5. But the recirculation zones in Fig. 8 were not obvious enough, and there was no reattachment point in -7<x/h< 0. Compared to the streamline contours of VCSA ratio=0.28, the primary and secondary recirculation zones of VCSA ratio=0.51 were near the step when the VCSA increased. It can be noticed that the distance between the first and secondary recirculation zone of VCSA ratio=0.28 was 3.3 cm which is longer than 2.72 cm of VCSA ratio=0.51. Further, the locations of the vortex core for VCSA ratio=0.28 were 0.83 cm and 1.88 cm, which were near the backward-facing step height than the lower VCSA ratio. In Figs. 8 and 9, no recirculation zone can be found in FFS flow. The VCSA ratio affects the formation of recirculation zones and the location of the reattachment point, which the higher VCSA ratio can cause the recirculation zone easily than the lower.

3.2.2. Velocity distribution

The vertical mean velocity distribution of FFS flow at x/h=17.3–22.3 and 13–18 and BFS flow at x/h =–5–0 in VCSA at 1 m^3/h for VCSA ratio=0.28 and 0.51 were depicted in Figs. 10 and 11,

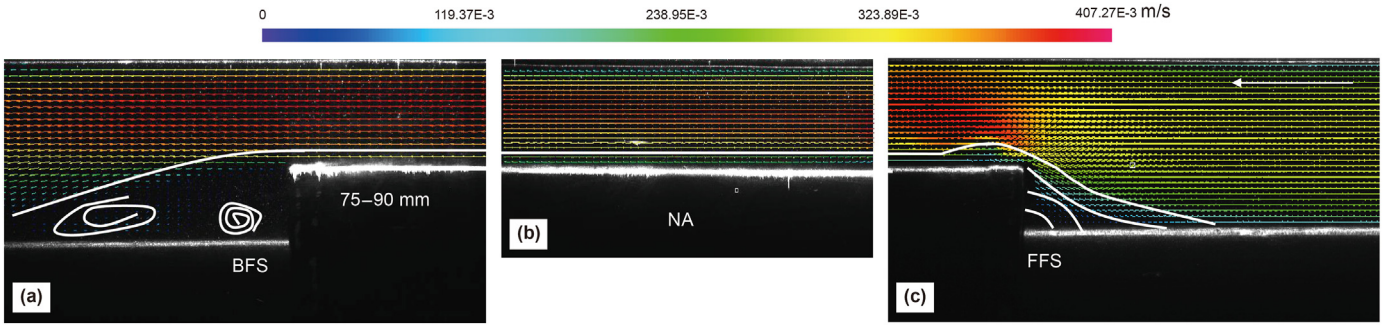

Fig. 4. 90–129 mm VCSA vector maps. (**a**) BFS flow. (**b**) NA flow. (**c**) FFS flow.

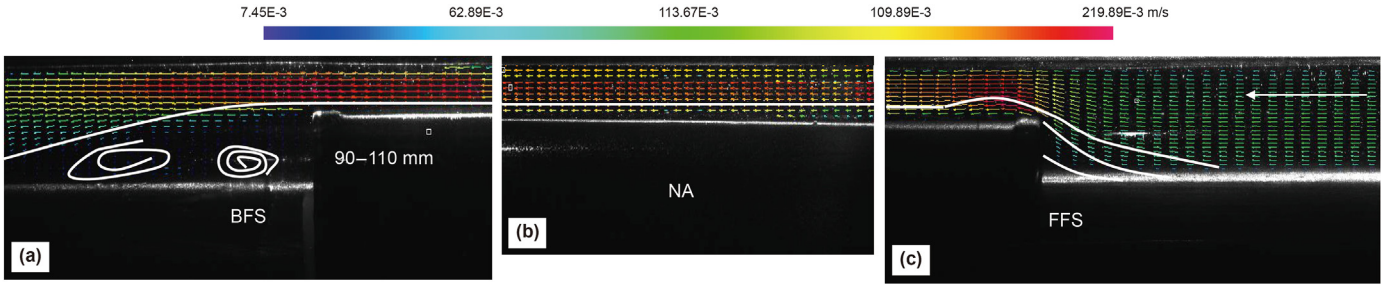

Fig. 5. 110–129 mm VCSA vector maps. (**a**) BFS flow. (**b**) NA flow. (**c**) FFS flow.

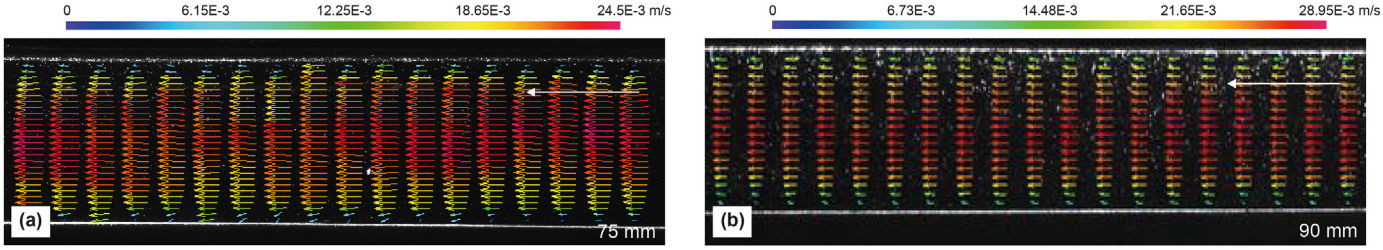

Fig. 6. Vector maps in smooth annular ducts. (**a**) 75 mm. (**b**) 90 mm.

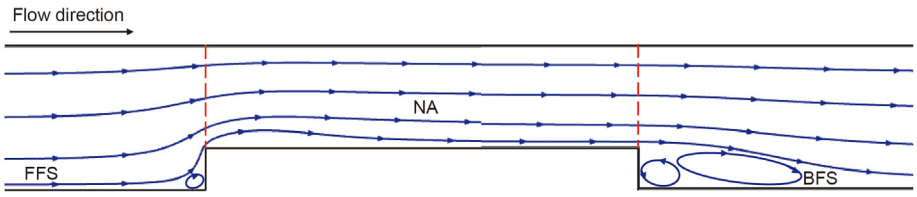

Fig. 7. The schematic diagram of the whole VCSA flow field model.

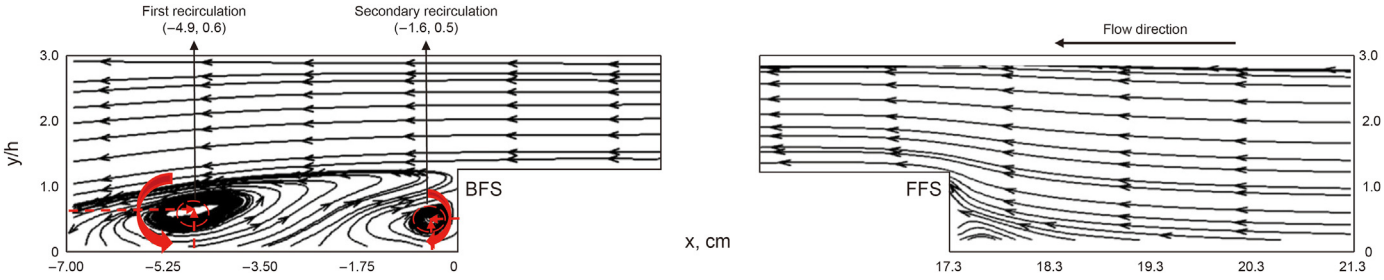

Fig. 8. BFS and FFS flow streamlines of VCSA ratio=0.28 at the flow rate of 1 m^3/h.

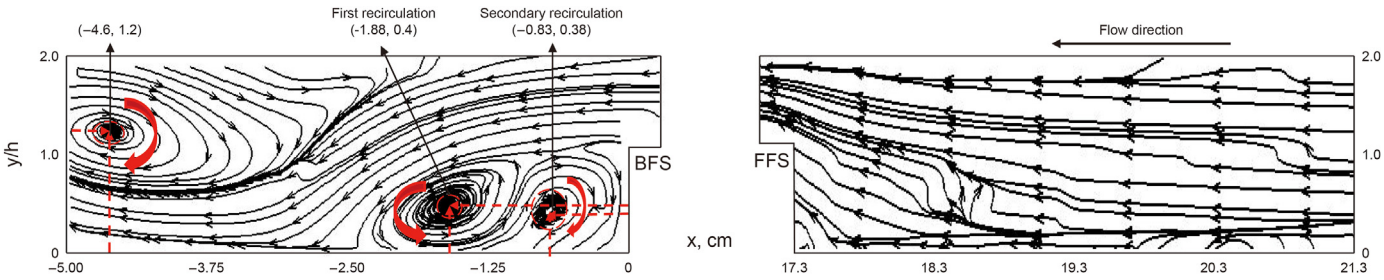

Fig. 9. BFS and FFS flow streamlines of VCSA ratio=0.51 at the flow rate of 1 m^3/h.

separately. In Figs. 10 and 11, it can be seen that the VCS structure had an acceleration effect, for the mean velocity of BFS was larger than the FFS flow above the step height (y/h>1.0) due to the narrow middle clearance. The vectors map also illustrated this phenomenon in Fig. 4~5. In Fig. 10, at y/h>1.0, the closer it to the step, the higher the mean velocity would be for both VCSA ratio=0.28 and 0.51, while it presented the opposite at y/h<1.0, which the flow was below the VCS height. The phenomenon illustrates that the VCS also has an inhibition effect on the velocity lower than the step height (y/h<1.0). The mean velocity decreased to the same value near y/h=1.0. The closer it was to the BFS, the mean velocity dropped more rapidly at y/h<1.0. It suggests that the VCSA ratio affects the distribution of mean velocity more seriously in BFS than FFS flow.

The flow field of BFS can be separated into two regions by the location near y/h=1.0 shown in Fig. 11a. The mean velocity of y/h>1.0 was larger than y/h < 1.0 and the velocity variation was increased at first then decreased at both y/h>1.0 and y/h<1.0. The mean velocity distributions of VCSA ratio=0.28 were similar at x/h=-5-0 along the X-axis direction. It illustrates that the main flow direction was basically parallel with the horizontal direction. Compared with Fig. 11a, the mean velocity distribution of VCSA ratio=0.51 in Fig. 11b was more complex due to the presence of the recirculation zone. It can be seen that the maximum velocity increased obviously along the X-axis direction and the y/h value also increased along the Y-axis direction due to the main flow being down to the bottom wall when it was far from the step.

The main component of the velocity was the dominant dynamic to the vortex generation, which was the main source of the local head losses. In order to directly reflect the main component velocity of the BFS flow, the profiles of velocity distributions of VCSA ratio=0.51 were analyzed through PIV obtained data. Fig. 12 illustrates that the value and variation trend of u velocity and mean velocity were almost the same. Therefore, u velocity was the main component of combined velocity, which the fluctuations of u velocity caused the main pressure losses rather than v velocity. Moreover, the VCS mainly suppressed the mean velocity by inhibiting axial velocity in BFS flow.

3.2.3. Turbulence characteristics

The FFS and BFS axial-turbulence intensity of VCSA ratio=0.28 and 0.51 flow at the flow rate of 1 m^3/h were depicted in Figs. 13 and 14. The turbulence intensity was critical to frictional pressure losses because it was the main component of turbulence kinetic energy (TKE), representing the energy possessed. Irregular turbulent fluctuations caused the increase of turbulence intensity so that the velocity fluctuations can cause more pressure losses. The definition of the axial-turbulence intensity and turbulent kinetic energy were given by Eq. (3) and Eq. (4):

$$u_{\mathrm{rms}} = \sqrt{\overline{u'u'}} \tag{3}$$

$$k = \frac{3}{2}(UI)^2 \tag{4}$$

where the rms is root mean square, u is the fluctuation velocity. U is the mean velocity and I is the turbulence intensity.

In Figs. 13 and 14, the magnitude of all quantities was relatively high in BFS flow compared to FFS flow and the axial-turbulence intensity was larger at y/h>1.0 than y/h<1.0. Globally, the peak of the turbulence was away from the step for the BFS flow but was near to the step for the FFS flow when the y/h increased. The peak of the turbulence intensity and the peak value range increased at the higher VCSA ratio, especially for BFS flow. It suggests that the VCSA ratio affects the axial-turbulence intensity values and the range of the turbulence intensity peak location. Understanding these energy consumptions is essential for reducing the frictional pressure losses of a VCSA duct by improving the geometry structures and fluid properties.

3.3. Effects of Reynolds number

3.3.1. Streamline distribution

Fig. 15 depicted the BFS and FFS flow streamlines in the X–Y plane of VCSA ratio=0.51 at Re=4799, 7999, and 10398. It can be noticed that the locations of recirculation zones were closely related to Re number, especially for BFS flow. Comparing the streamline, both the first and secondary recirculation zones were closer to the step. The length of the recirculation zone also increased in streamwise at a higher Re number. In spanwise, the y/h value of the secondary recirculation zone decreased which the

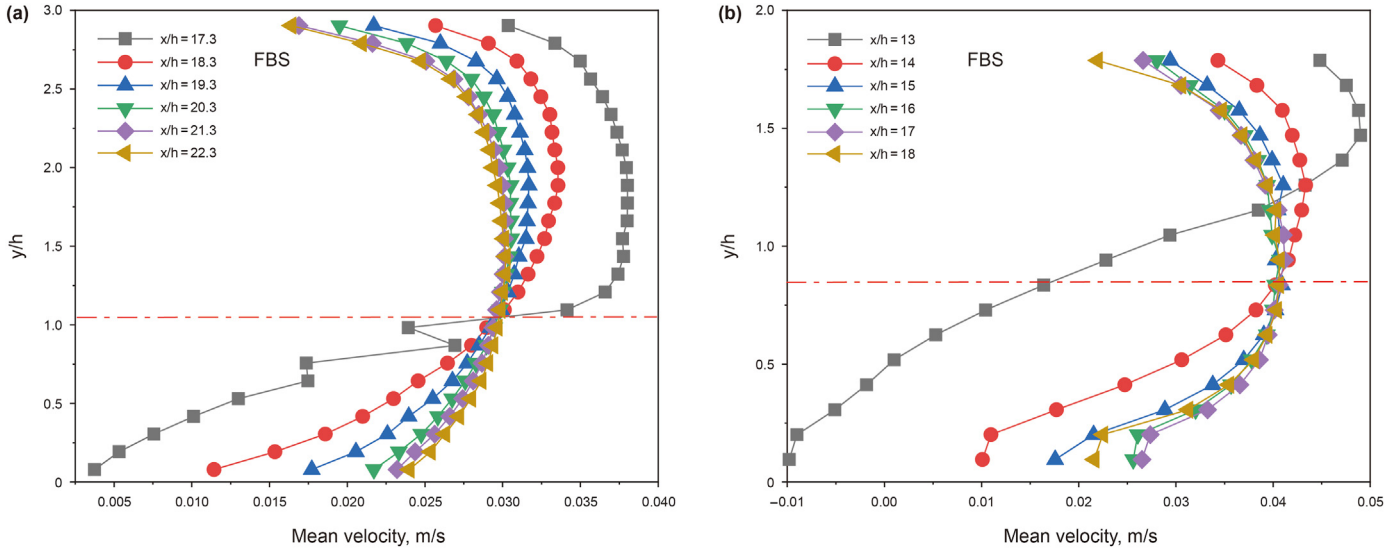

Fig. 10. FFS vertical profiles of streamwise mean velocity of VCSA ratio = 0.28 and 0.51 at the flow rate of 1 m^3/h. (**a**) VCSA ratio = 0.28. (**b**) VCSA ratio = 0.51. (The x/h=17.3 and x/h=13 are the locations of the front end for 75–90 mm and 90–110 mm VCS, respectively).

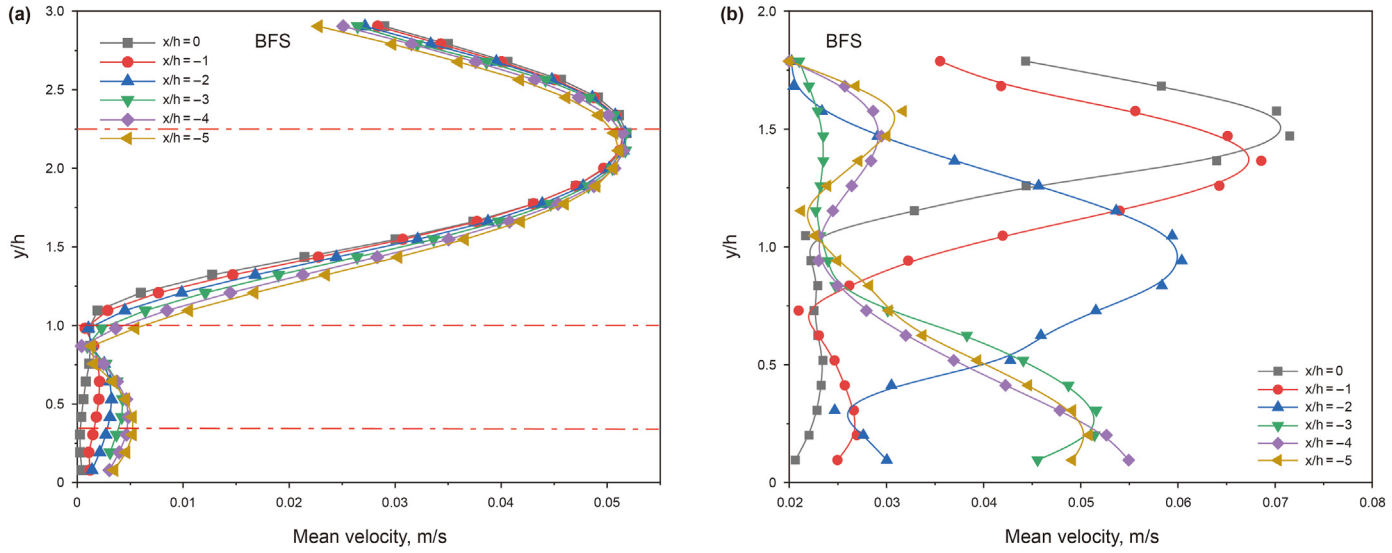

Fig. 11. BFS vertical profiles of streamwise mean velocity of VCSA ratio = 0.28 and 0.51 at the flow rate of 1 m^3/h. (**a**) VCSA ratio = 0.28. (**b**) VCSA ratio = 0.51. (The x/h=0 is the location of the back end for 75–90 mm and 90–110 mm VCS).

vortex structure was closer to the step corner with the increased Re number. It can be inferred that the reattachment length was longer with the higher Re number, though the details were not shown in Fig. 15 due to the CCD scope limitation. It was shown in Fig. 15a that the secondary recirculation region at the step corner was not obvious at a low Re. This was due to the lower Re number, the weaker energy the fluid had, and the energy cannot generate the secondary recirculation vortex structure.

3.3.2. Velocity distribution

The vertical mean velocity distribution of FFS and BFS flow of VCSA ratio=0.51 at x/h=17.3–22.3 and -5-0 at Re=4799,7999,10398 were depicted in Figs. 16 and 17, separately. Compared with Fig. 16, it found that the influence of Re number on velocity was mainly on BFS flow, especially the location of y/h>1.0 in **Fig. 17**. At x/h=0, -2, -4, it can be seen clearly that in all positions, the velocity first increased rapidly and then decayed gradually to the same velocity when it peaked, finally increased slightly.

The mean velocity distribution along Y-axis could not reflect the streamwise mean velocity changes of BFS flow intuitively, therefore, the X-axis distribution of mean velocity, u velocity, and v velocity profiles at Re=4799, 7999, and 10398 were analyzed as shown in Fig. 18. It suggests that the Re number mainly affected u velocity distribution and the main component of the mean velocity was still u velocity. Re number did not affect the variation trend of velocity and it only changed the velocity value at different regions.

3.3.3. Turbulence characteristics

The FFS and BFS flow axial-turbulence intensity of VCSA ratio=0.51 for different y/h values at Re=4799, 7999, and 10398 were compared in Figs. 19 and 20, respectively. Globally, the axial-turbulence intensity increased with the increased Re numbers at all locations. The peak of the turbulence intensity and the length of peak value range increased at the higher Re number for both FBS and BFS flow. In Fig. 19, it can be seen that the peak of FFS turbulence intensity was closer to the step for y/h=0.5 and farther away from the step for y/h=1.5. And the peak of BFS turbulence intensity was closer to the step for y/h>1.0 and farther away from the step for y/h<1.0 shown in Fig. 20. The influence of Re number on the axial-turbulence intensity of y/h>1.0 was more significant than y/h<1.0, especially for a higher Re number.

3.4. Vorticity-based POD analysis

In many experimental studies, snapshot POD (proper orthogonal decomposition) analysis is a widely used method to reveal coherent structure due to the fact that vorticity is Galilean invariant. The time series of velocity vector fields are linearly decomposed into a finite number of modes in Eqs. (5) and (6). Large-scale in turbulent flows can be represented in predominant modes and the small-scale can be represented by higher modes with a lower amplitude of lower energy content. The snapshot POD decomposes the original flow field into a series of spatially orthogonal modes based on the energy-based hierarchy of the modes (Ma et al., 2021).

$$\boldsymbol{U} = \overline{\boldsymbol{U}} + \sum_{i=1}^{N} \Phi_i a_i^T \tag{5}$$

$$\Phi = [\varphi_1 \varphi_2 \ldots \varphi_n] \tag{6}$$

Where, $\boldsymbol{U}$ is the original velocity vector field, and $\overline{\boldsymbol{U}}$ is a time-averaged flow. Φ_i is a linear combination of spatial orthogonal modes and a_i^T are POD coefficients. All the POD modes are ranked in a decreased order by the eigenvalues to ensure the first modes contain high energy, while the higher modes correspond to less energy.

In this paper, POD was applied to the vorticity field, which was calculated from the PIV velocity data. The vorticity-based POD is more efficient in highlighting vorticity fields, for the POD reconstruction can extract key flow features and remove turbulence background. The snapshots method provides several modes equal to the number of snapshots. For clarity, the plot was limited only to the first 30 modes, containing about 75% of the energy in Fig. 21 both at Re=7999 and 10398. The eigenvalues were normalized with respect to their sum, representing the total turbulent energy of the fluctuations. The maximum eigenvalue corresponded to Mode 1 that described large-scale vortices. It was seen that the eigenvalues decreased rapidly after Mode 2. Some modes higher than 30 also corresponded to some small-scale vortex structures and some seemed to be noise. The first mode eigenvalue became more significant with the increase of Re numbers due to the mode obtaining more energy in a turbulent flow.

To aid the visualization of flow characteristics, vorticity was

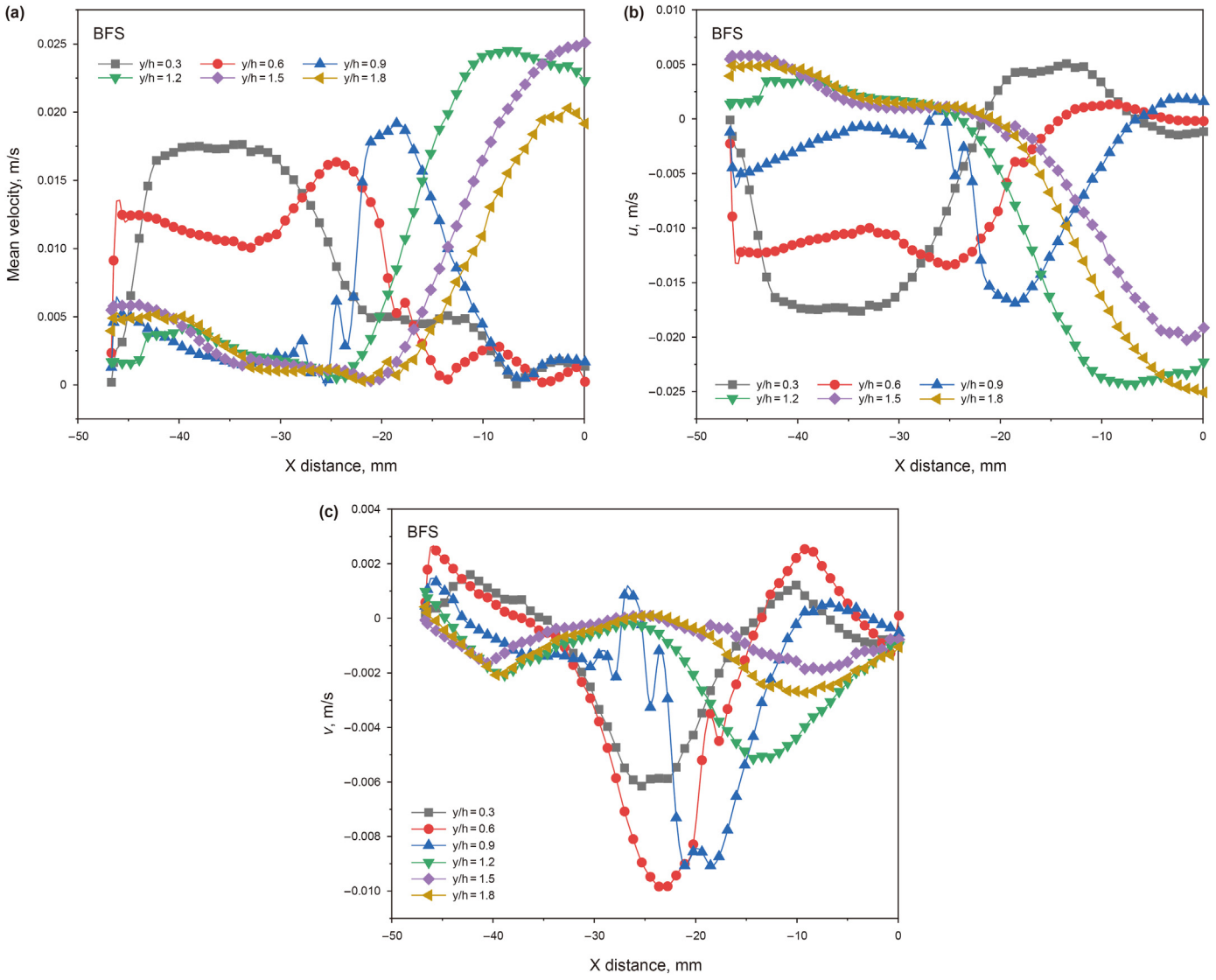

Fig. 12. BFS horizontal profiles of velocity distributions of VCSA ratio=0.51 at the flow rate of 1 m^3/h. (**a**) Mean velocity. (**b**) *u* velocity. (**c**) *v* velocity.

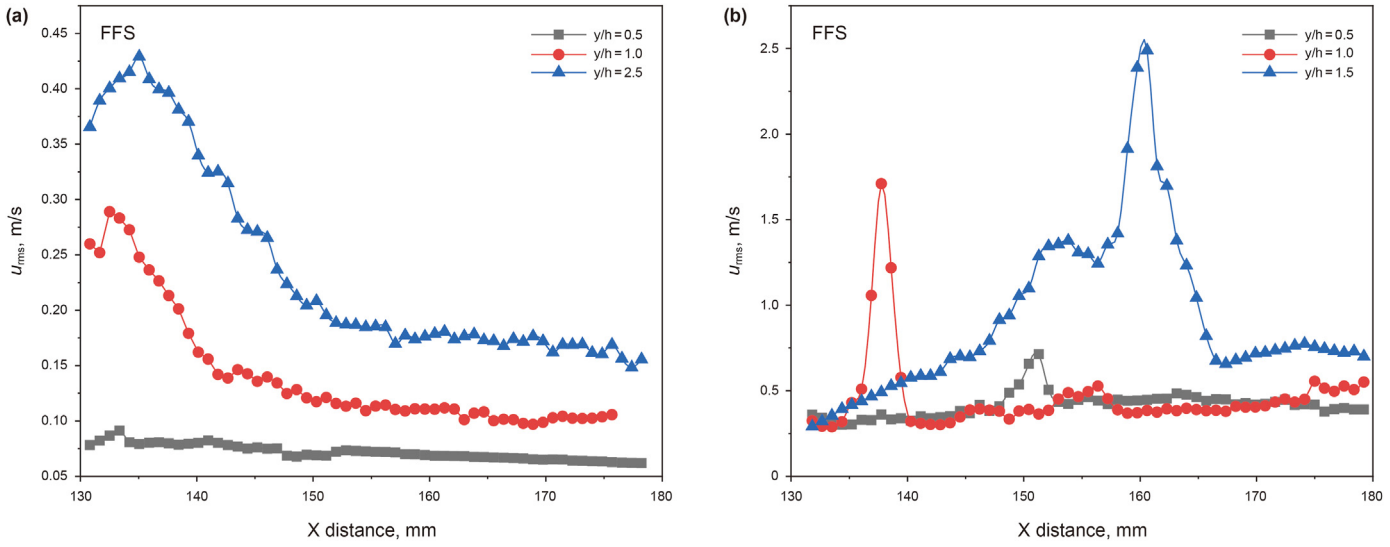

Fig. 13. Axial-turbulence intensity profiles of FFS for VCSA ratio =0.28 and 0.51 at the flow rate of 1 m^3/h. (**a**) VCSA ratio =0.28. (**b**) VCSA ratio=0.51

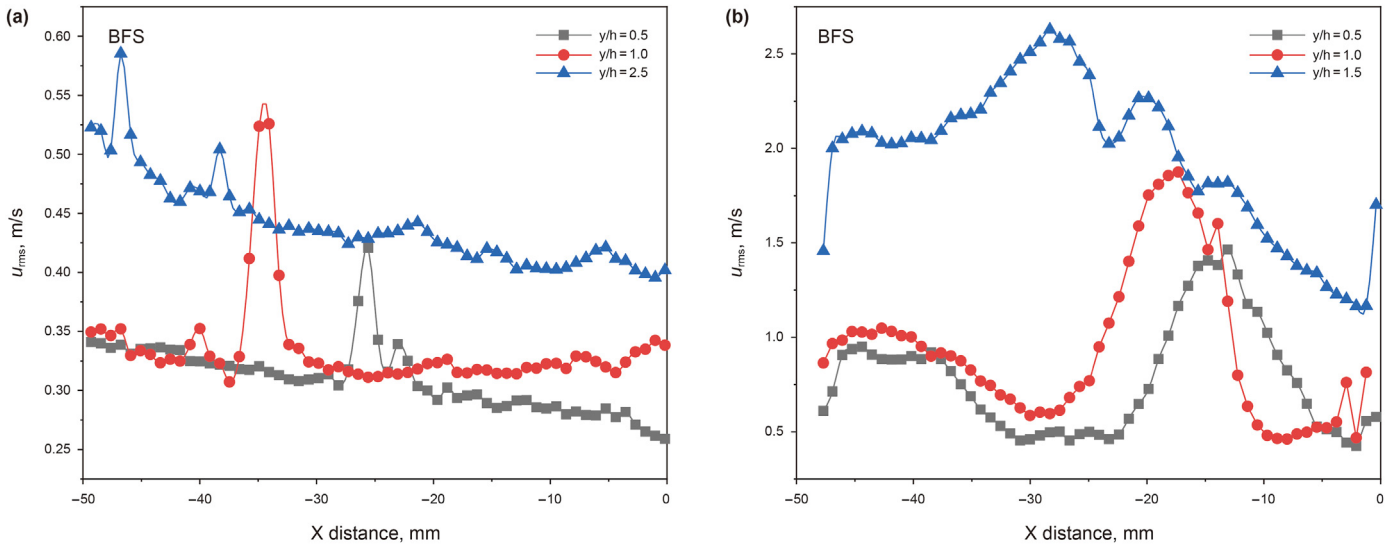

Fig. 14. Axial-turbulence intensity profiles of BFS for VCSA ratio=0.28 and 0.51 at the flow rate of 1 m^3/h. (**a**) VCSA ratio=0.28. (**b**) VCSA ratio=0.51.

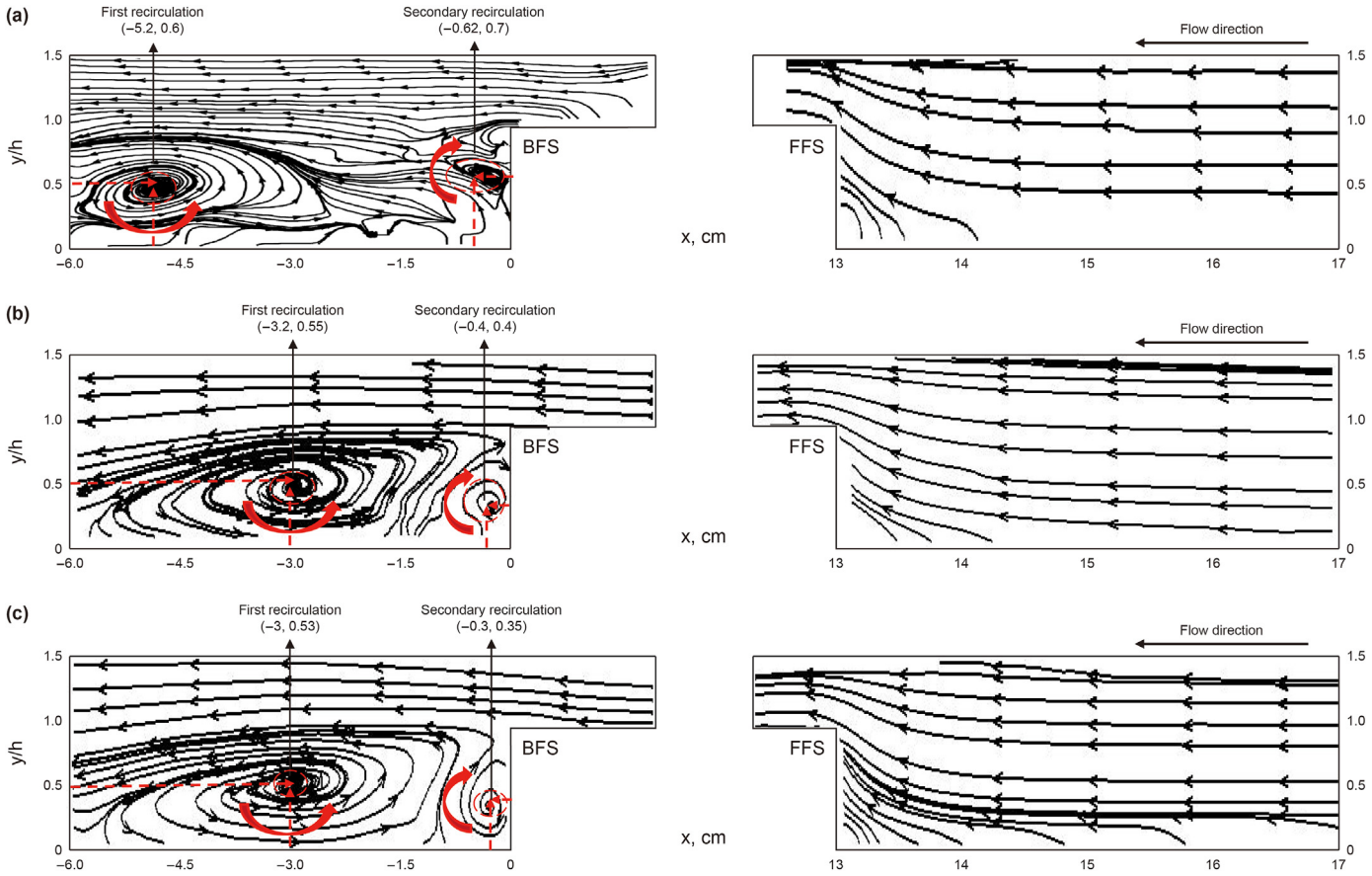

Fig. 15. BFS (left) and FFS (right) streamlines of VCSA ratio=0.51 at different Re numbers. (a) Re=4799. (b) Re=7999. (c) Re=10398.

computed in normalized for the corresponding spatial modes. Figs. 22 and 23 showed mean vorticity contours and the first POD mode of BFS flow, respectively. The first mode described precisely and corresponded with high accuracy mean vorticity field of flow and almost reconstructed all large-scale structures, while vortex structures were distinguished on the second and the higher modes. The lower POD modes corresponded to small-scale vortices (von Karman vortices), which accumulated a larger fraction of energy. To observe vortex structure clearly, Fig. 24 a-h showed the vorticity contour lines of Mode 2, Mode 3, Mode 5, and Mode 10 obtained from vorticity-based POD analysis. The contour lines showed that the small-scale structures were mainly occupied on the upper wall

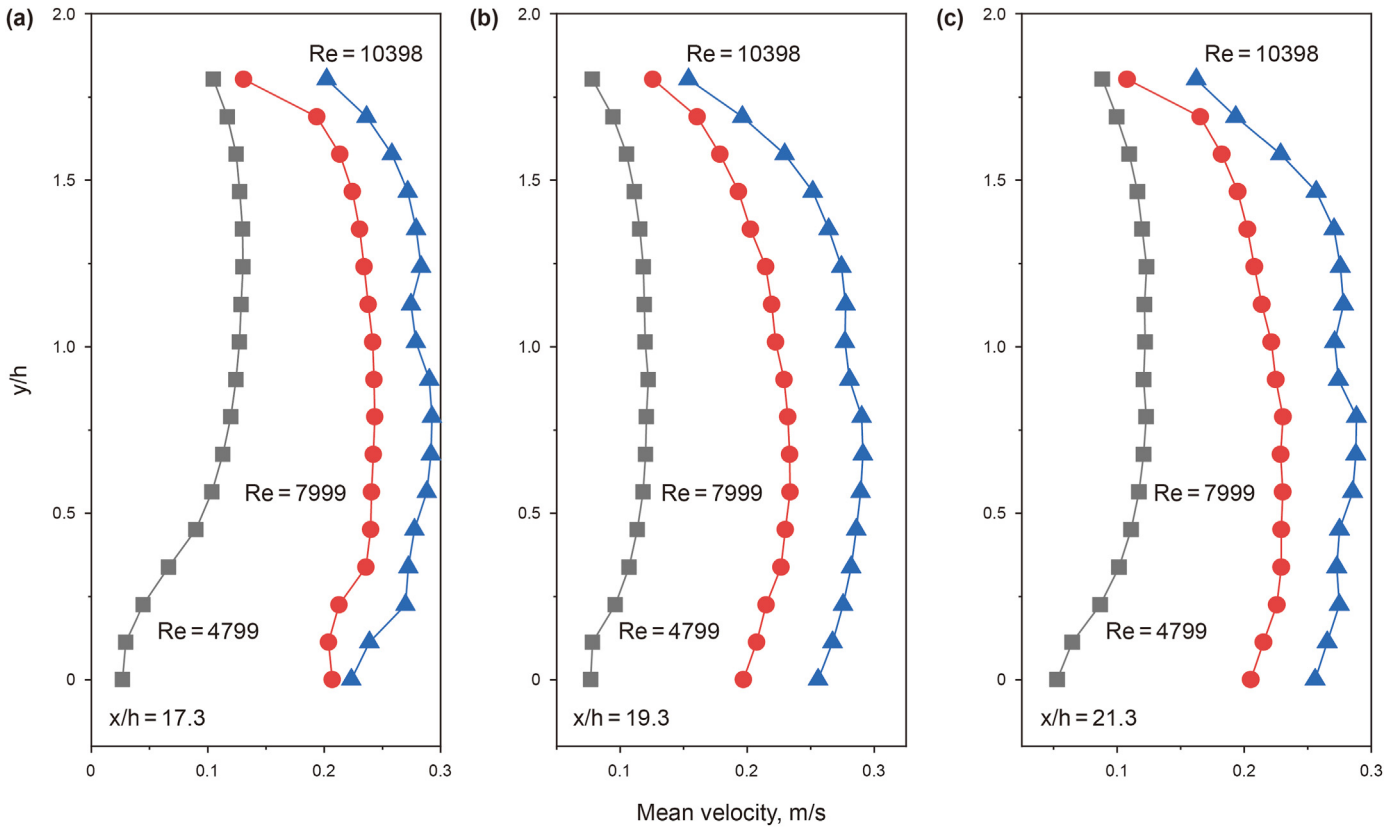

Fig. 16. FFS vertical profiles of streamwise mean velocity at different Re numbers. (a) x/h = 0. (b) x/h=−2. (c) x/h=−4. (The x/h=17.3 is the location of the front end for VCS).

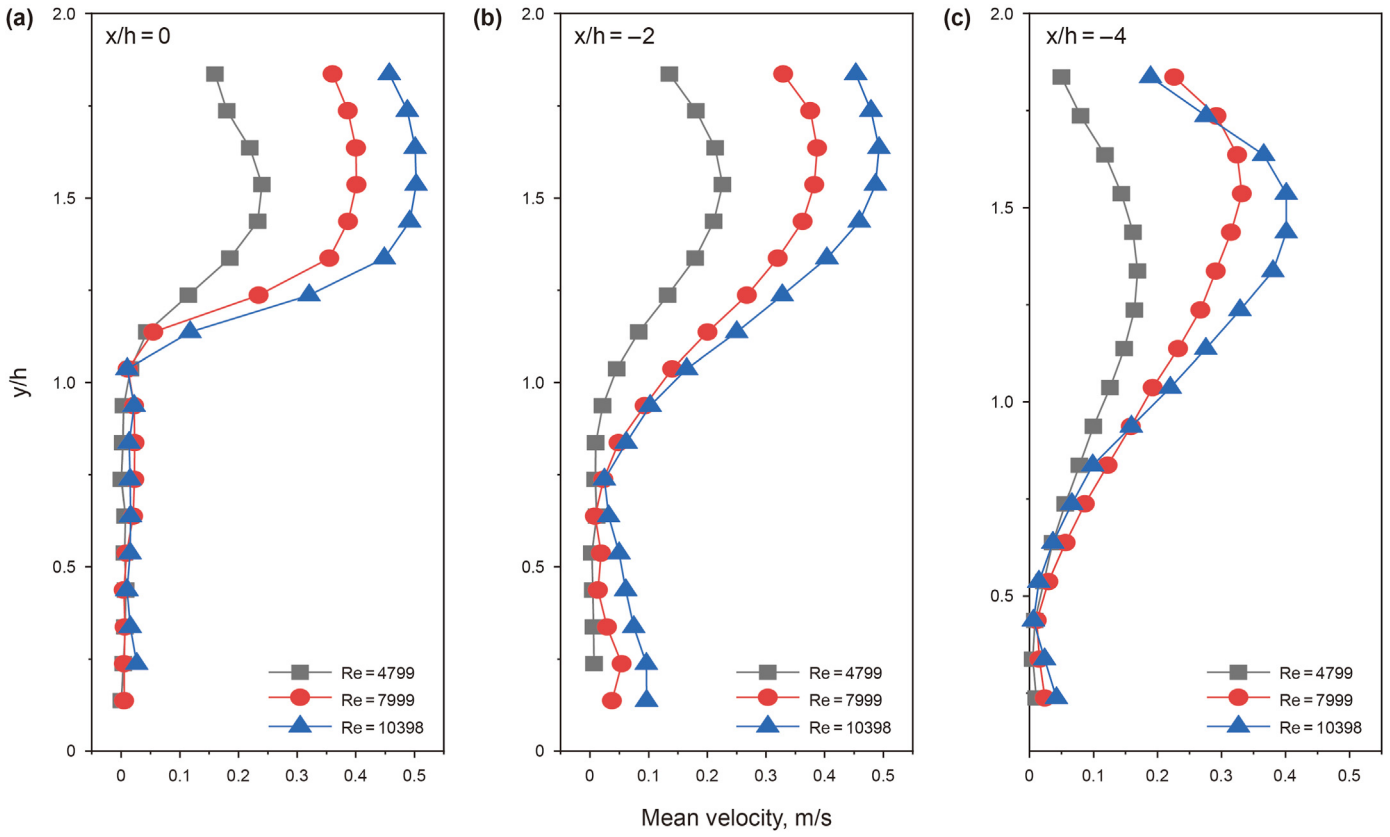

Fig. 17. BFS vertical profiles of streamwise mean velocity at different Re numbers. (a) x/h=0. (b) x/h=−2. (c) x/h=−4.

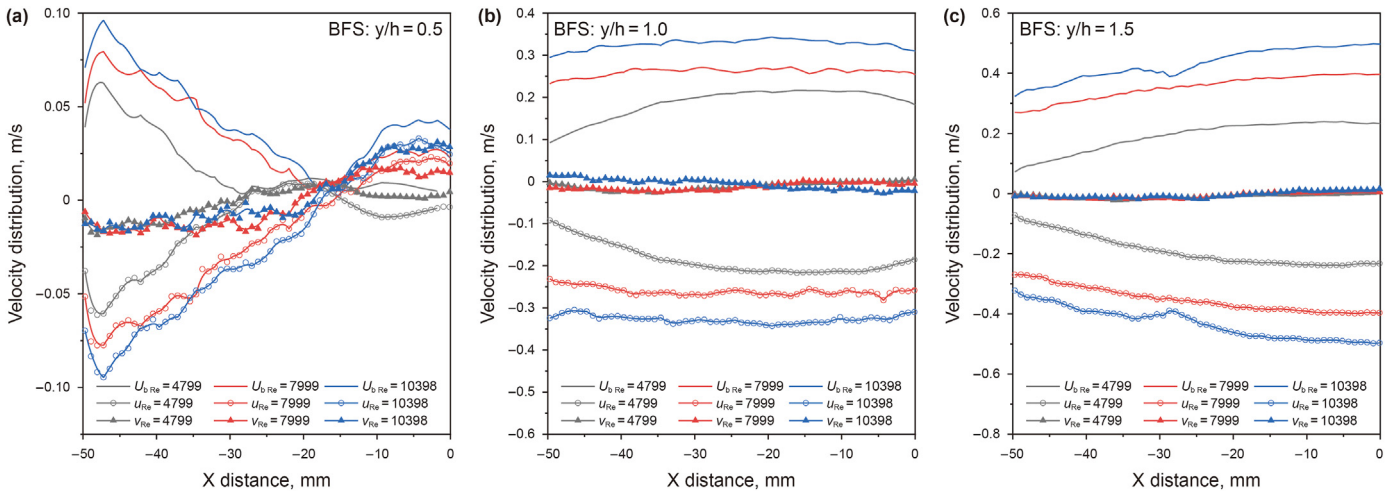

Fig. 18. The mean velocity, *u* and *v* velocity distribution of VCSA ratio=0.51 for different y/h values at Re= 4799, 7999 and 10398. (a) y/h=0.5. (b) y/h=1.0. (c) y/h=1.5.

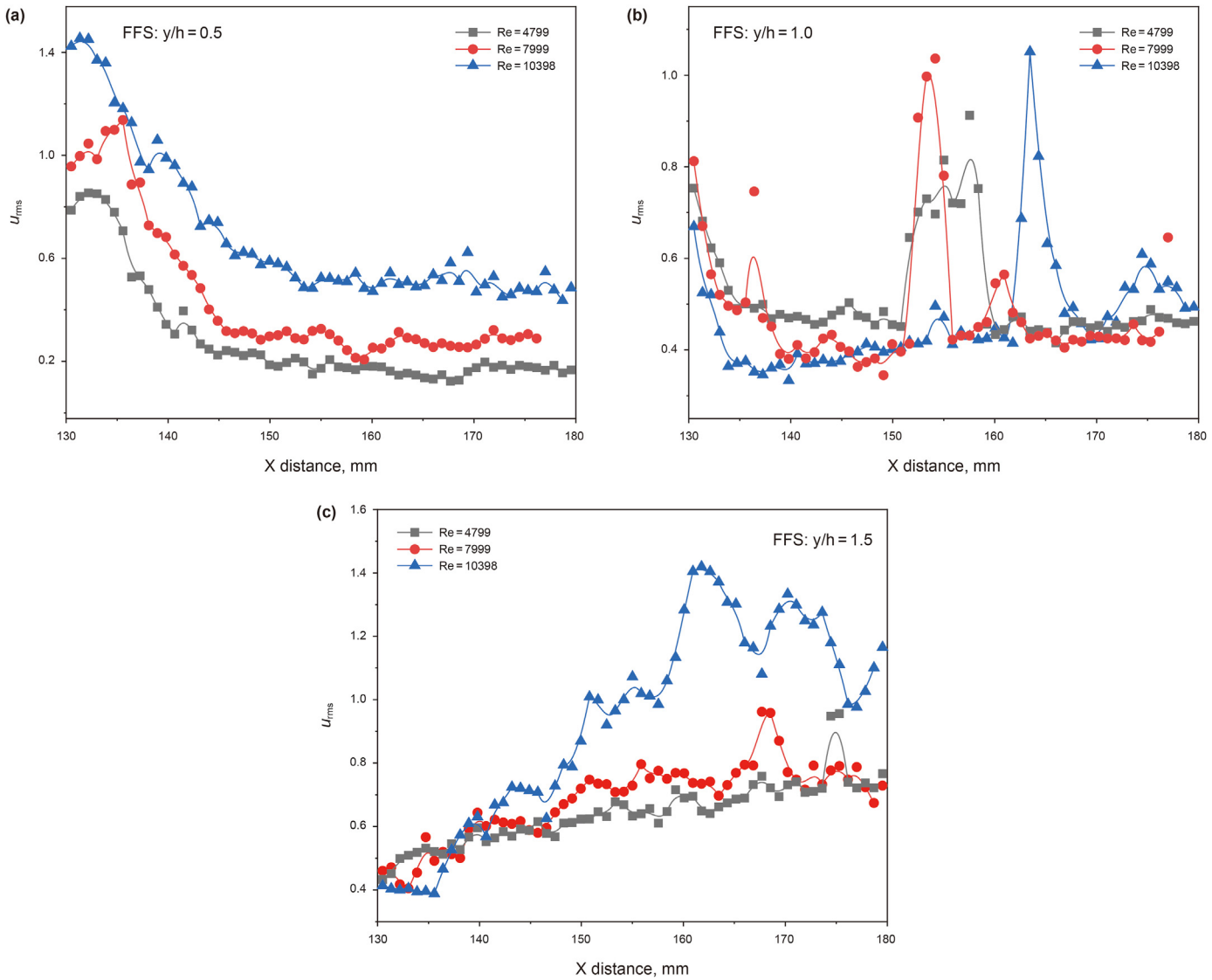

Fig. 19. FFS axial-turbulence intensity at different y/h positions in X–Y plane. (a) y/h=0.5. (b) y/h=1.0. (c) y/h=1.5.

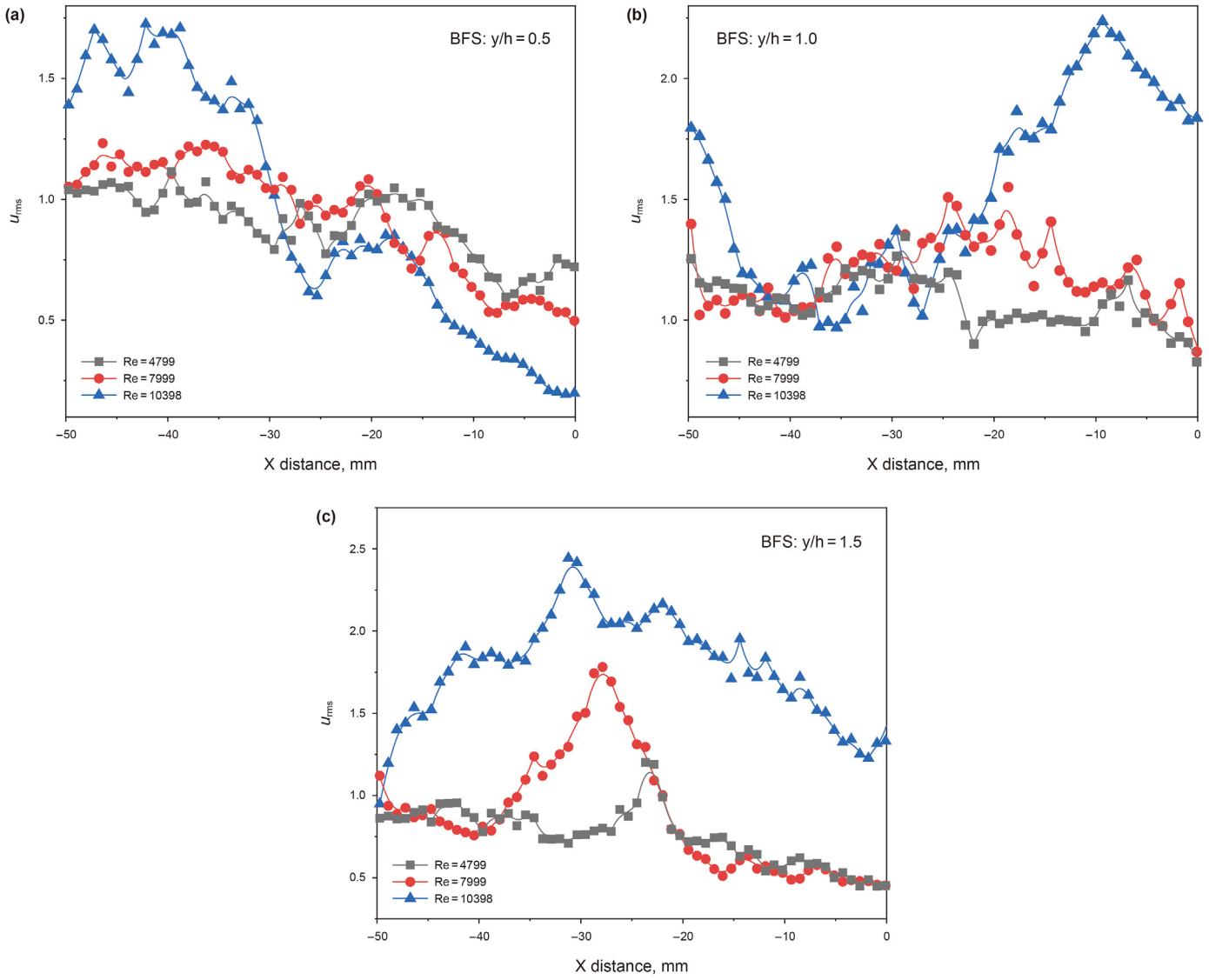

Fig. 20. BFS axial-turbulence intensity at different y/h positions in X–Y plane. (a) y/h=0.5. (b) y/h=1.0. (c) y/h=1.5.

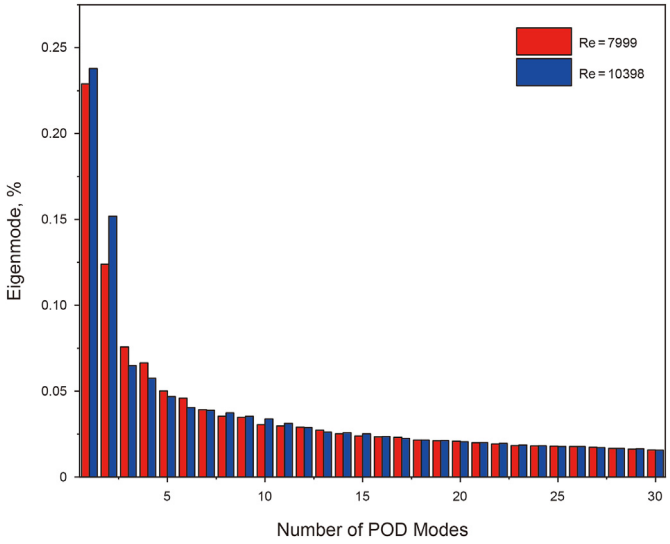

Fig. 21. Energy distribution of the first 30 POD modes.

boundary and near y/h=1.5, both above the step height, especially in a higher mode. Figs. 13 and 14 (in Sec.3.2) also illustrated this phenomenon. The number of small-scale structures increased at the same POD modes at a higher Re number.

The POD coefficients reflected the temporal dependence between the POD modes and instantaneous flow fields as weighting factors. Fig. 25 plotted the time's history of the POD coefficient of the first 2 modes obtained from over 200 snapshots at Re=7999 and Re=10398, separately. In Fig. 25, it can be seen clearly that the first two modes were periodic and accompanied by a small phase difference. This structure also represented the relationship of the cyclic changes of the first two modes, which means different stages of the same structure (Meyer et al., 2007). The relationship was more apparent, and the weight of Mode 1 was higher with the increased Re numbers.

A time-dependent coefficients plot can reflect the importance of two different modes for a given snapshot by POD. Fig. 26 showed the coefficients of Mode 2 versus Mode 1 at Re=7999 and Re=10398. It indicates that the existence of low-dimensional dynamics in the downstream of forward-backward facing step in an annular pipe by the closed nature of the resulting diagram in Fig. 21.

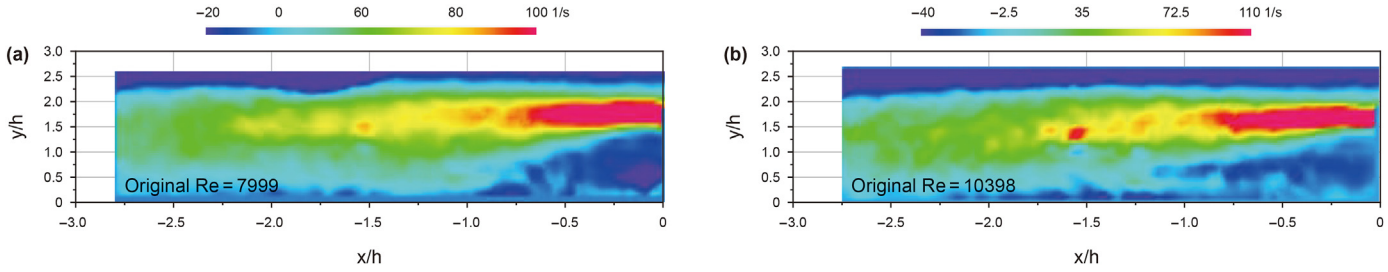

Fig. 22. Vorticity contours of BFS flow for VCSA=0.28. (a) Re=999. (b) Re=10398.

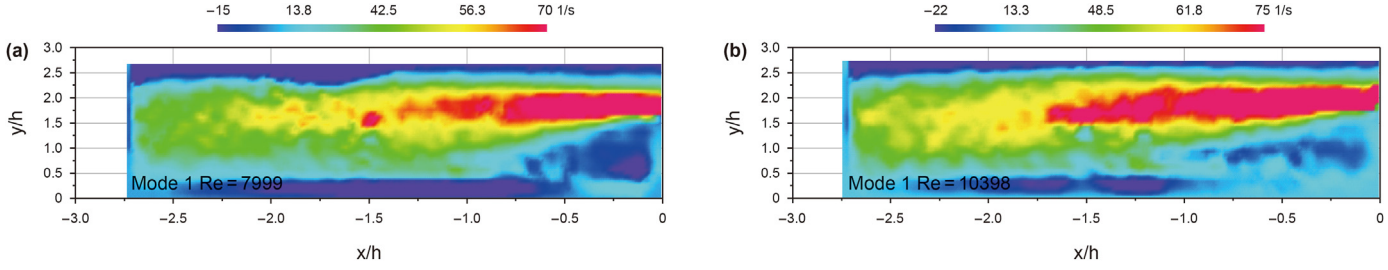

Fig. 23. Reconstruction vorticity contours of POD Mode 1 in BFS flow for VCSA ratio=0.28.(a) Re=7999. (b) Re=10398.

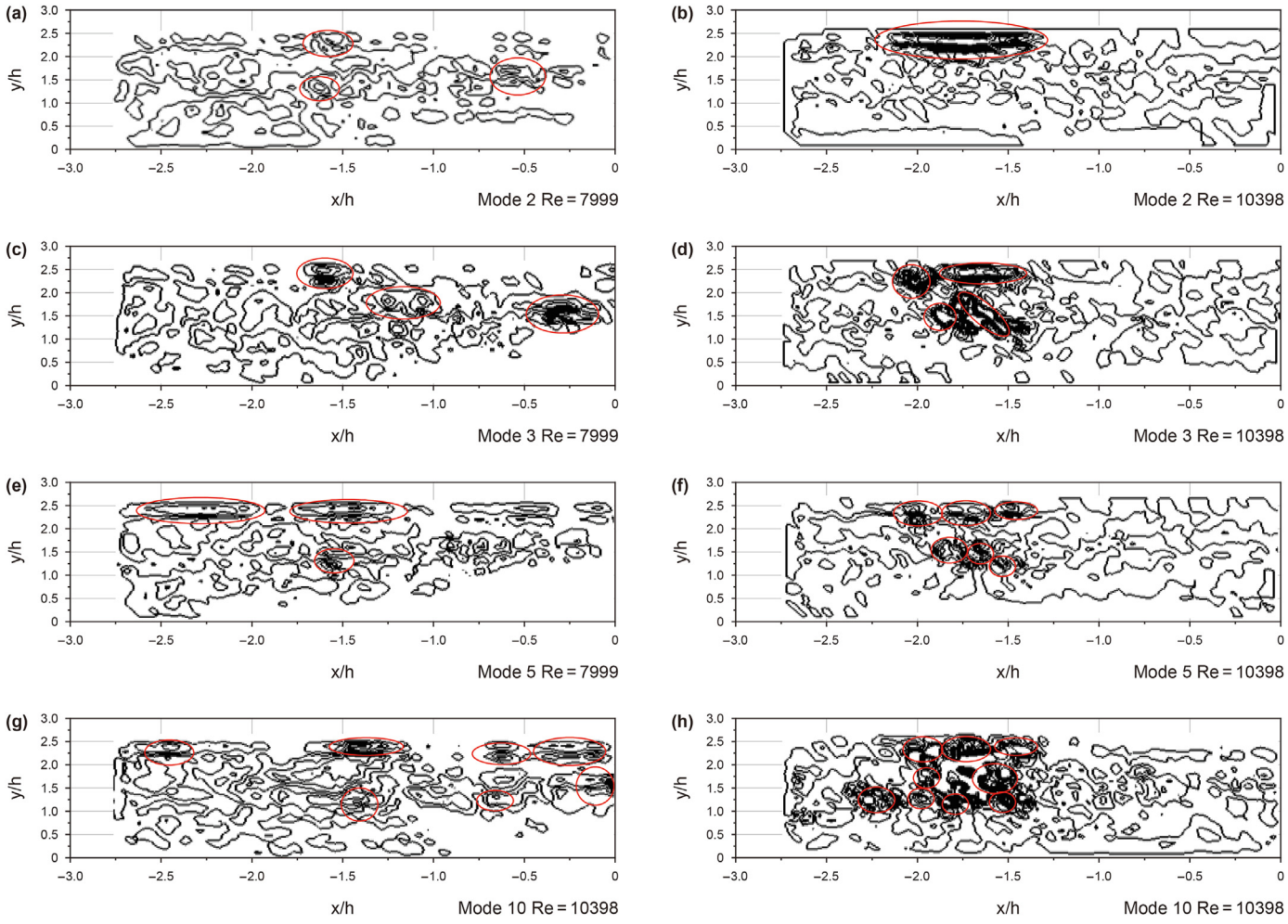

Fig. 24. Vorticity contour lines of the first 10 POD modes at Re=7999 (left) and Re=10398 (right). (**a**–**b**) Mode 2. (**c**–**d**) Mode 3. (**e**-**f**) Mode 5. (**g**–**h**) Mode 10.

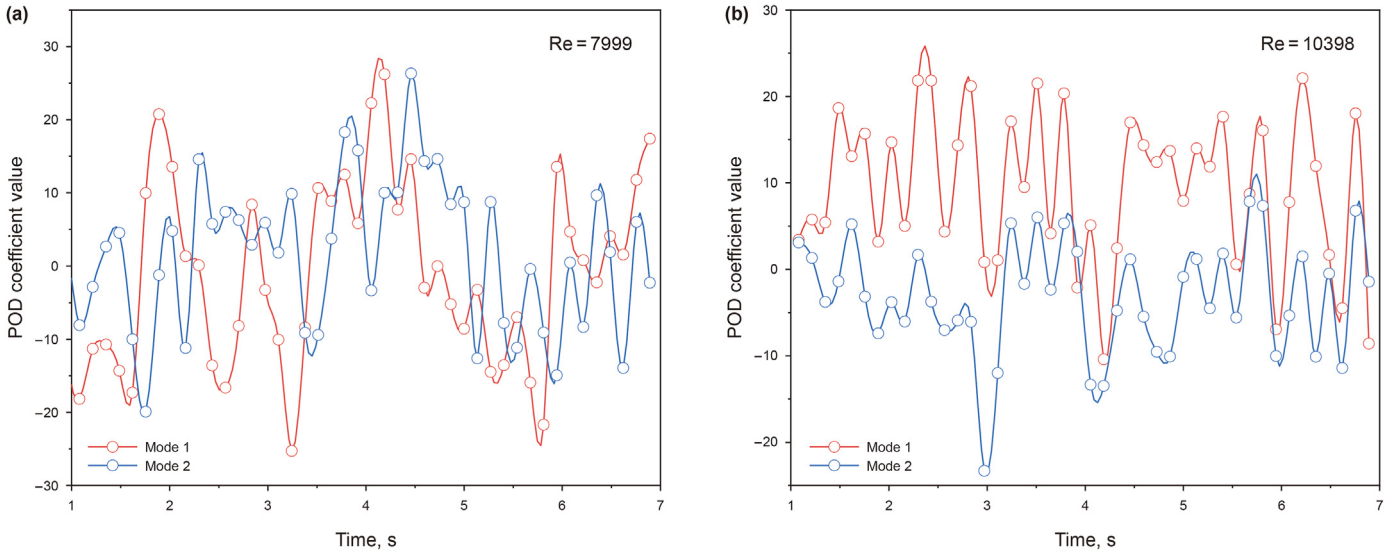

Fig. 25. POD coefficients of the first two modes.

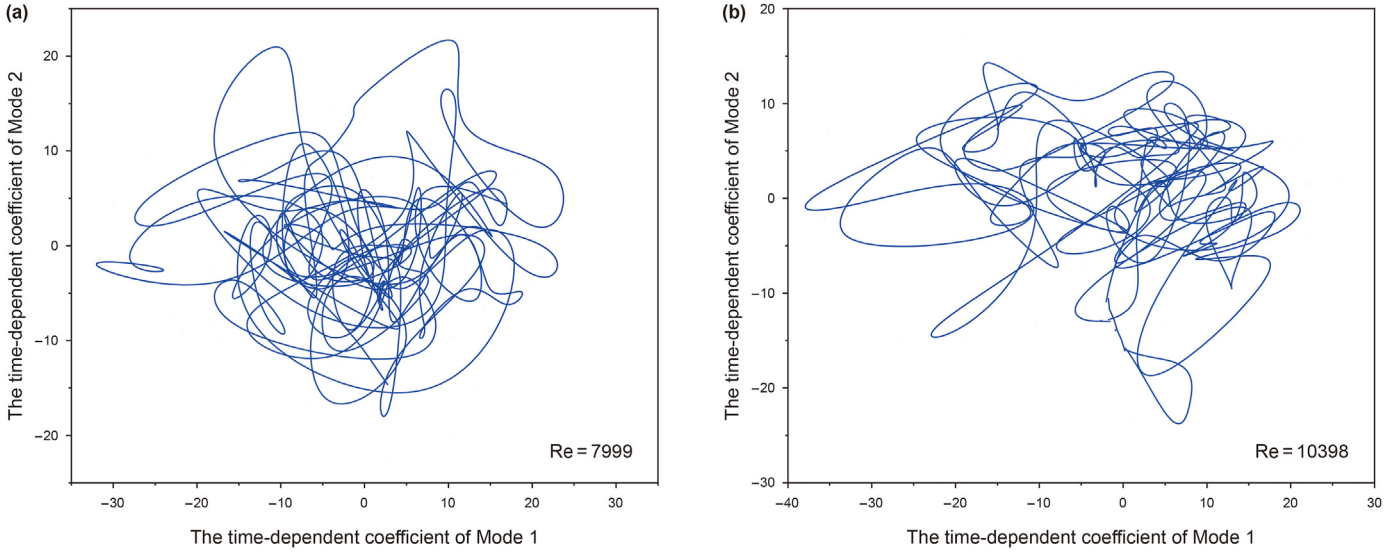

Fig. 26. Correlation maps of the first two POD mode coefficients for the system at different Re numbers. (**a**) Re=7999. (**b**) Re=10398.

The projection revealed low-dimensional dynamics in the form of cycling behavior. The low-dimensional characteristic (Tinney et al., 2006) in the azimuthal plane was that most of the energy (around 50%) was contained in the first and second POD modes in turbulent sudden expansion flows. Low dimensionality in a flow suggests that reduced models can be developed to describe it and to design appropriate control systems (Mak and Balabani, 2007). With the existence of low dimensionality, a low number of POD modes can capture the overall characteristics of the motion. Such behavior was also reported for swirling flow past a sudden expansion and blockage flow (Mak and Balabani, 2007; Yuan et al., 2020). Low dimensionality was observed in the VCSA flow in the present study and it proves that the downstream flow characteristics in variable cross-section annular are similar to the sudden expansion and swirling flow.

4. Conclusions

In this paper, tubing collars' influence on hydrodynamics behavior of annular duct has been investigated by experimental using PIV. Effects of VCSA ratio, inflow Reynolds number on the flow characteristics have been analyzed. And the vorticity field has been revealed by POD method. The major conclusions are listed as follows:

(1) The generation of recirculation zones in BFS flow is more accessible than FFS flow and the size of recirculation zones of BFS flow are larger than FFS flow. The visualization flow field proves that the local head losses due to sudden contraction are larger than the sudden expansion in a VCSA flow.

(2) The VCSA ratio has a more obvious effect on the distribution of mean velocity and turbulence intensity in BFS flow than FFS flow. The VCSA ratio affects the formation of recirculation zones and the location of the reattachment point in BFS flow. The higher VCSA ratio can cause the recirculation zone more easily than the lower.
(3) The main component velocity of VCSA flow is the axial velocity at different Re numbers and VCSA ratios. The velocity and turbulence intensity are all increased with the increased Re numbers. The Re number influences the peak value location of the velocity and turbulence intensity in BFS and FFS flow.
(4) The VCS structure has an inhibition effect on the velocity lower than the step height ($y/h<1.0$), and has an acceleration effect on the velocity higher than the step height ($y/h>1.0$).
(5) The streamwise large-scale coherent structures are revealed at the first mode by POD, which are predominant the main characteristics of the BFS flow. The small-scale structures are mainly occupied on $y/h>1.0$, above the step height, especially in higher modes.
(6) The exhibition of low-dimensional was observed in the sudden expansion area of the VCSA flow.

It would be interesting to extend the present investigation by using different properties fluids and higher Reynolds numbers with a primary interest in a vital parameter, the frictional pressure loss, since the prediction of this parameter plays a significant role in petroleum engineering. Moreover, future works focusing on analyzing the influence of the variable cross-section annular flow characteristics on the pressure losses can be encouraged. This work will help precisely predict the frictional pressure losses in drilling and completion, fracture, workover, etc.

Acknowledgments

The authors are grateful for the financial support of the National Key R&D Program of China (No. 2019YFB1504102), the National Natural Science Foundation of China (52020105001) and the National Science Fund for Distinguished Young Scholars (51725404) and their approval of publishing this paper.

References

Abu-Mulaweh, H.I., 2009. Investigations on the effect of backward-facing and forward-facing steps on turbulent mixed-convection flow over a flat plate. Exp. Heat Tran. 22 (2), 117–127. https://doi.org/10.1080/08916150902805927.
Addad, Y., Laurence, D., Talotte, C., Jacob, M.C., 2003. Large eddy simulation of a forward–backward facing step for acoustic source identification. Int. J. Heat Fluid Flow 24 (4), 562–571. https://doi.org/10.1016/S0142-727X(03)00050-X.
Araújo, J.D.P., Miranda, J.M., Campos, J.B.L.M., 2013. Simulation of slug flow systems under laminar regime: hydrodynamics with individual and a pair of consecutive Taylor bubbles. J. Petrol. Sci. Eng. 111, 1–14. https://doi.org/10.1016/j.petrol.2013.10.007.
Birchenko, V.M., Usnich, A.V., Davies, D.R., 2010. Impact of frictional pressure losses along the completion on well performance. J. Petrol. Sci. Eng. 73 (3–4), 204–213. https://doi.org/10.1016/j.petrol.2010.05.019.
Bizhani, M., Kuru, E., 2018a. Assessment of the equivalent sandbed roughness and the interfacial friction factor in hole cleaning with water in a fully eccentric horizontal annulus. SPE J. 23, 1748–1767. https://doi.org/10.2118/191133-PA.
Bizhani, M., Kuru, E., 2018b. Critical review of mechanistic and empirical (Semi mechanistic) models for particle removal from sandbed deposits in horizontal annuli with water. SPE J. 23 (2), 237–255. https://doi.org/10.2118/187948-PA.
Bui, B., 2012. Modeling the effect of pipe rotation on pressure loss through tool joint. In: SPETT Energy Conference and Exhibition, 11-13 June, Port-of-Spain, Trinidad. https://doi.org/10.2118/157982-MS.
Cartalosu, D., Dupuis, D., 1993. An analysis accounting for the combined effect of drillstring rotation and eccentricity on pressure losses in slimhole drilling. In: SPE/IADC Drilling Conference, vols. 22–25. February, Amsterdam, Netherlands. https://doi.org/10.2118/25769-MS.
Chalmers, H., Fang, X., Tachie, M.F., 2020. Streamwise aspect ratio effects on turbulent flow separations induced by forward–backward-facing steps. ASME. J. Fluids Eng. 143 (2), 21305. https://doi.org/10.1115/1.4048686.
Dokhani, V., Ma, Y., Li, Z., Geng, Tie, Yu, M., 2020. Effects of drill string eccentricity on frictional pressure losses in annuli. J. Petrol. Sci. Eng. 187, 106853. https://doi.org/10.1016/j.petrol.2019.106853.
Enfis, M., Ahmed, R., Saasen, A., 2011. The hydraulic effect of tool-joint on annular pressure loss. In: SPE Production and Operations Symposium. March, Oklahoma City, Oklahoma, USA, pp. 27–29. https://doi.org/10.2118/142282-MS.
Eren, T., 2018. Drilling of horizontal wells in carbonate reservoirs of Middle East for petroleum production – investigation of hydraulics for the effect of tool joints. Hittite Journal of Science & Engineering 5 (3), 239–247. https://doi.org/10.17350/HJSE19030000103.
Eren, T., Merey, S., Can, P., 2021. Effect of casing couplings to frictional pressure losses while setting casing a step change. In: SPE/IADC Middle East Drilling Technology Conference and Exhibition, 25–27 May. UAE, Abu Dhabi. https://doi.org/10.2118/202082-MS.
Fang, X., Tachie, M., 2019. Flows over surface-mounted bluff bodies with different spanwise widths submerged in a deep turbulent boundary layer. J. Fluid Mech. 877, 717–758. https://doi.org/10.1017/jfm.2019.617.
Hemphill, T., Bern, P.A., Rojas, J., Ravi, K., 2007. Field validation of drillpipe rotation effects on equivalent circulating density. In: SPE Annual Technical Conference and Exhibition, 11-14 November, Anaheim, California, U.S.A. https://doi.org/10.2118/110470-MS.
Hirpa, M.M., Arnipally, S.K., Bizhani, M., Kuru, E., Gelves, G., Ibrahim, A.R., 2020. Effect of particle size and surface properties on the sandbed erosion with water flow in a horizontal pipe. SPE J. 25, 1096–1112. https://doi.org/10.2118/199875-PA.
Hirpa, M.M., Ergun, K., 2020. Hole cleaning in horizontal wells using viscoelastic fluids: an experimental study of drilling-fluid properties on the bed-erosion dynamics. SPE J. 25, 2178–2193. https://doi.org/10.2118/199636-PA.
Huang, Z.W., Li, G.S., Huang, Z., 2015. Experiments on pressure loss along casing-tubing annulus. J. China Univ. Petrol. 39 (1), 79–82. https://doi.org/10.3969/j.issn.1673-5005.2015.01.011.
Jeong, Y., Subhash, N.S., 2004. Analysis of tool joint effects for accurate friction pressure loss calculations. In: IADC/SPE Drilling Conference, vols. 2–4. March, Dallas, Texas. https://doi.org/10.2118/87182-MS.
Kaushik, V.V.R., Sumana, G., Gargi, D., Prasanta, K.D., 2012. CFD simulation of core annular flow through sudden contraction and expansion. J. Petrol. Sci. Eng. 86–87, 153–164. https://doi.org/10.1016/j.petrol.2012.03.003.
Li, X.J., Chen, B., Luo, X.W., Zhu, Z.C., 2020. Effects of flow pattern on hydraulic performance and energy conversion characterisation in a centrifugal pump. Renew. Energy 151, 475–487. https://doi.org/10.1016/j.renene.2019.11.049.
Ma, X.Y., Tang, Z.Q., Nan, J., 2021. Investigation of spanwise coherent structures in turbulent backward-facing step flow by time-resolved PIV. Exp. Therm. Fluid Sci. 132, 110569. https://doi.org/10.1016/j.expthermflusci.2021.110569.
Mak, H., Balabani, S., 2007. Near field characteristics of swirling flow past a sudden expansion. Chem. Eng. Sci. 62, 6726–6746. https://doi.org/10.1016/j.ces.2007.07.009.
Malah, H., Chumakov, Y.S., Sadeghian, E., 2021. The effects of the cross-section shape of the surface-mounted cylinder on the free convective junction flow. Eng. Sci and Tech. 27, 101004. https://doi.org/10.1016/j.jestch.2021.05.008.
Ma, Y., Mohebbi, R., Rashidi, M.M., Yang, Z., Fang, Y., 2020. Baffle and geometry effects on nanofluid forced convection over forward- and backward-facing steps channel by means of lattice Boltzmann method. Phys. Stat. Mech. Appl. 554, 124696. https://doi.org/10.1016/j.physa.2020.124696.
Meyer, K.E., Pedersen, J.M., Özcan, O., 2007. A turbulent jet in crossflow analysed with proper orthogonal decomposition. J. Fluid Mech. 583 (25), 199–227. https://doi.org/10.1017/S0022112007006143.
Orlik, E., Bocharov, O., Gavrilov, A., 2020. Numerical simulation of non-Newtonian hydrodynamics in an annular channel with tool joint. J. Phys. Conf. 1677 (1). https://doi.org/10.1088/1742-6596/1677/1/012194.
Qin, K., Di, Q.F., Zhou, X., He, Y.Z., Wang, W.C., Chen, F., Zhang, H., 2021. Nonlinear dynamic characteristics of the drill-string for deep-water and ultra-deep water drilling. J. Petrol. Sci. Eng. 209, 109905. https://doi.org/10.1016/j.petrol.2021.109905.
Rodolfo, M.P., William, M.V., Jorge, L.B., Natan, A.V.B., William, D.P.F., Marcelo, S.C., Erick, M.F., Antonio, C.B., 2021. Flow visualization in centrifugal pumps: a review of methods and experimental studies. J. Petrol. Sci. Eng. 203, 108582. https://doi.org/10.1016/j.petrol.2021.108582.
Sachidananda, B., Arun, K.S., 2021. Effect of inlet shear on turbulent flow past a wall-mounted finite-size square cylinder. Ocean Eng. 234, 109270. https://doi.org/10.1016/j.oceaneng.2021.109270.
Sazhin, O., 2021. Gas outflow into vacuum over a forward- and backward-facing step in a wide range of rarefaction. Int. J. Heat Mass Tran. 179, 121666. https://doi.org/10.1016/j.ijheatmasstransfer.2021.121666.
Simoes, S.Q., Miska, S.Z., Takach, N.E., Mengjiao, Y., 2007. The effect of tool joints on ECD while drilling. In: Production and Operations Symposium, 31 March-3 April. Oklahoma City, USA. https://doi.org/10.2118/106647-MS.
Tinney, C.E., Glauser, M.N.E.L., Eaton, J.A., 2006. Taylor Low dimensional azimuthal characteristics of suddenly expanding axisymmetric flows. J. Fluid Mech. 567, 41–155. https://doi.org/10.1017/S0022112006002527.
Vajargah, A.K., Fard, F.N., Parsi, M., Hoxa, B.B., 2014. Investigating the impact of the "Tool Joint Effect" on equivalent circulating density in deep-water wells. In: SPE Deepwater Drilling and Completions Conference. September, Galveston, Texas, USA. https://doi.org/10.2118/170294-MS.
Veeresh, T., Venkatasubbaiah, K., 2021. Numerical investigation on the extrusive and intrusive subcavity types and their location on the primary recirculation

zone for the supersonic turbulent flow through cavity type flame holders. Therm. Sci. Eng. Prog. 25, 100987. https://doi.org/10.1016/j.tsep.2021.100987.
Viloria, O., Marilyn, 2006. Analysis of Drilling Fluid Rheology and Tool Joint Effect to Reduce Errors in Hydraulics Calculations. Texas A&M University Doctoral dissertation. https://hdl.handle.net/1969.1/4334.
Wang, H.G., Bai, Y.M., 1998. Laboratory study on pressure in annular of slim hole. Oil Dril. Product. Technol. 20 (4), 9–15. https://doi.org/10.3969/j.issn.1000-7393.1998.04.002.
Woyciekoski, M.L., Endres, L.A.M., de Paula, A.V., Möller, S.V., 2020. Influence of the free end flow on the bistability phenomenon after two side by side finite height cylinders with aspect ratios of 3 and 4 and high blockage. Ocean Eng. 195, 106658. https://doi.org/10.1016/j.oceaneng.2019.106658.
Yang, D., Sun, B., Xu, T., Liu, B., Li, H., 2021. Experimental and numerical study on the flow and heat transfer characteristic of nanofluid in the recirculation zone of backward-facing step microchannels. Appl. Therm. Eng. 199, 117527. https://doi.org/10.1016/j.applthermaleng.2021.117527.
Yao, L.M., Liu, J.B., Li, X.Y., Yue, Q.B., Liu, Y.X., Wang, H.T., 2019. Application of the building block approach to characterize the pressure loss of water and fracturing fluid in contraction-expansion pipe. J. Petrol. Sci. Eng. 176, 51–61. https://doi.org/10.1016/j.petrol.2018.12.010.
Yuan, B., Zhang, Y., Liu, L., Wei, J., 2020. Flow boiling heat transfer and associated bubble behaviors over backward- and forward-facing steps. Exp. Therm. Fluid Sci. 122, 110300. https://doi.org/10.1016/j.expthermflusci.2020.110300.
Yuan, D.D., Deng, J., Han, R., Li, D.Y., Tan, S.C., 2020. Experimental study on flow structures of central blockage accidents in a rectangular channel using PIV and POD. Ann. Nucl. Energy 153, 108037. https://doi.org/10.1016/j.anucene.2020.108037.
Zhu, N., Huang, W.J., Gao, D.L., Deng, F.Y., 2021. The hydraulic effect of tool joints on open-hole extended-reach limit model. In: 55th U.S. Rock Mechanics/Geomechanics Symposium, 18-25 June. Virtual. In: https://onepetro.org/ARMAUSRMS/proceedings/ARMA21/All-ARMA21/ARMA-2021-1106/467857.